Mechanism and Machine Theory 178 (2022) 105083

Contents lists available at ScienceDirect

Mechanism and Machine Theory

journal homepage: www.elsevier.com/locate/mechmt

A compliant-mechanism-based lockable prismatic joint for high-load morphing structures

Yinjun Zhao [a,b], Guangbo Hao [b,*], Luguang Chai [b], Yingzhong Tian [a], Fengfeng Xi [c]

[a] School of Mechatronic Engineering and Automation, Shanghai Key Laboratory of Intelligent Manufacturing and Robotics, Shanghai University, Shanghai 200444, China
[b] School of Engineering and Architecture-Electrical and Electronic Engineering, University College Cork, Cork, Ireland
[c] Department of Aerospace Engineering, Toronto Metropolitan University, Toronto, ON M5B 2K3, Canada

ARTICLE INFO

Keywords:
Lockable joints
Compliant mechanisms
Morphing structures
PZT actuation
Static modeling
Parametric optimization

ABSTRACT

Lockable joints are widely used in robotic systems and adaptive structures for energy management and/or topology reconfiguration. However, it is still challenging to design a joint with desired properties, including high locking load, infinite locking positions, short switching time, energy-efficient control, and a compact and lightweight structure. This paper aims at this open problem by presenting a novel piezoelectric (PZT) actuated lockable prismatic joint. This joint is a compliant mechanism (CM) consisting of a compound bridge-type compliant mechanism (CBCM) and a pair of compound multibeam parallelogram mechanisms (CMPMs). It can produce the required input/output stiffness to transmit large forces for high-load locking. It can also provide a desired input/output motion range for PZT actuation-based unlocking and for facilitating preloading adjustment. An analytical model is presented based on a compliance matrix method and the nonlinear model of the CMPM to predict the joint's static characteristics under various input/output conditions. A two-step optimization framework is proposed for locking applications. The theoretical study and nonlinear FEA/experimental verification confirm the feasibility of the design and the accuracy of the proposed model.

1. Introduction

Lockable devices are a kind of key components in robotic systems [1] and adaptive structures [2,3], which can be utilized to achieve energy management and/or structure reconfiguration. In parallel robots, lockable devices could change their topology to vary stiffness characteristics [4]. In serial robots, lockable devices could reconfigure their geometries [5] or lock their shapes to perform different tasks [6]. For a geometry variable truss system, lockable devices can be used to achieve its reconfiguration between a truss and a mechanism [7,8]. In nature, flying at no-mechanical-energy-cost can be observed in albatross through an elbow-lock system [9,10].

An ideal lockable device should have a large locking force, an infinite amount of locking positions, a short switching time, an energy-efficient control, and a compact and lightweight structure [1]. Although many designs of lockable mechanisms have been put forward, and the principles are well established, it is still an open issue to design a lockable device that could fulfill all of the above requirements.

Four main principles can be used to design a lockable device, including mechanical [6,11-13], friction [14,15], singularity [16],

* Corresponding author.
E-mail address: g.hao@ucc.ie (G. Hao).

https://doi.org/10.1016/j.mechmachtheory.2022.105083
Received 4 April 2022; Received in revised form 20 July 2022; Accepted 27 August 2022
Available online 12 September 2022

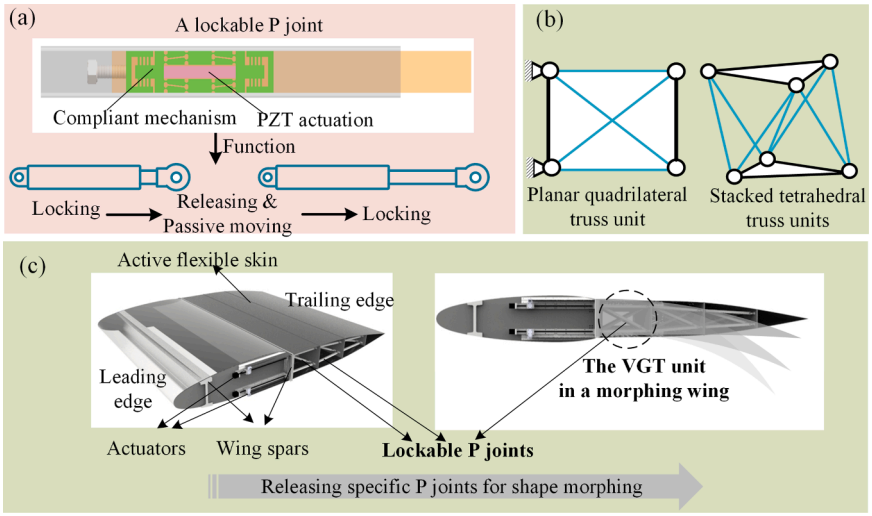

Fig. 1. Functions of the proposed design and one of its applications. (a) A PZT actuated lockable P joints design. (b) Its application in the variable geometry truss units. (c) One of the applications in morphing airfoil wings [29].

and material-based locking [17,18]. Traditional mechanisms are often combined with traditional actuations for mechanical implementation. Those traditional mechanisms includes ratchets [11], hydraulic cylinders/valves [6,13], cam mechanisms [19], and four-bar linkages [20,21]. Those traditional actuations can be indicated by electromagnetic [5,22], hydraulic [6,13], and pneumatic actuators [23]. Generally speaking, the combination of the traditional mechanisms and actuations leads to a complex electromechanical system for locking, which is inconvenient to assemble and has a large weight and design space. Especially when a system requires many lockable devices, it creates more challenges. Although the material-based locking can use a variable stiffness material to lock, such as shape memory polymer, it has a limited locking capacity and is therefore only suitable for miniaturized hold-release scenarios [17,18]. In other applications, the long response time and the creeping of the variable stiffness material are still unsolved problems.

Many new lockable joint designs have been recently proposed to meet more stringent requirements, such as the design space, weight, and load-carrying ability, in some unique and emerging fields. Guo et al. proposed a small self-locking ratch mechanism actuated pneumatically for a variable stiffness soft gripper [24]. Yang et al. [25] proposed a shape memory alloy actuated leverage-type locking mechanism to realize the stiffness adjustment of continuum robotics. Lin and Guo [7] presented several concept designs of self-locking composite joints using a friction-based self-locking principle, which aims to design high payload reconfigurable parallel robots such as *in-situ* robots and legged mobile landers. These joints can be designed by multi-link mechanisms, screw thread sliders and cam clampers. Moosavian et al. [13] proposed a multifunctional self-circulating hydraulic cylinder for orientation controllable locking in aerospace applications.

A new modular lockable prismatic (P) joint is presented in this paper as shown in Fig. 1(a), to fill the gap in prior art and meet our design requirements. It has a compact and lightweight structure, a high load-carrying ability, and is easy to assemble and fabricate. The P joint can be easily used to construct reconfigurable topology units (as shown in Fig. 1(b)), serving for a wide range of potential applications such as space or aerospace morphing systems, parallel robots, and backbones for continuum robots [26–28]. One of the immediate applications of our design is the reconfigurable variable geometry truss (VGT) systems presented in [2,29]. In this application, many compact and lightweight lockable P joints are needed to construct a passive lockable load-bearing structure for an adaptive trailing edge. Different kinds of motion modes can be obtained by releasing specific joints to make the trailing edge reach desired shapes through active skins actuation, as shown in Fig. 1(c) [29].

The lockable P joint consists of a mechanism and an actuation. CMs are adopted since they have many advantages compared with conventional rigid-body mechanisms, such as part-count reduction, reduced assembly time, simplified manufacturing processes, increased precision, reduced wear, and reduced weight [30]. The smart martial actuation is selected because it is more conducive to the miniaturization and lightweight of the system. Furthermore, it is also easy to control, given the lockable function's simplicity (just locking and releasing). As long as we provide enough input signal excitation to the actuation material to generate enough actuation force and displacement, the devices could function well without having to precisely control the actuation's deformation through sensors and complex controllers.

This study uses a simple friction-based locking principle and designs a mechanism with a large input and output stiffness to improve the normal contact force. We propose to combine a CBCM [31] with CMPMs [32] to realize our mechanical design. The piezoelectric stack (PZT) is selected for actuation since its large blocking force, high stiffness, and rapid response characteristics. Though its travel stroke is tiny, which is around 0.1% and 0.2% length of the PZT stack [33], a CBCM as a displacement amplifier could overcome this problem. More design considerations and explanations of the working principle will be presented in the next section.

In this study, an analytical model is developed to evaluate the motion and force transmission properties of the CBCM under motion

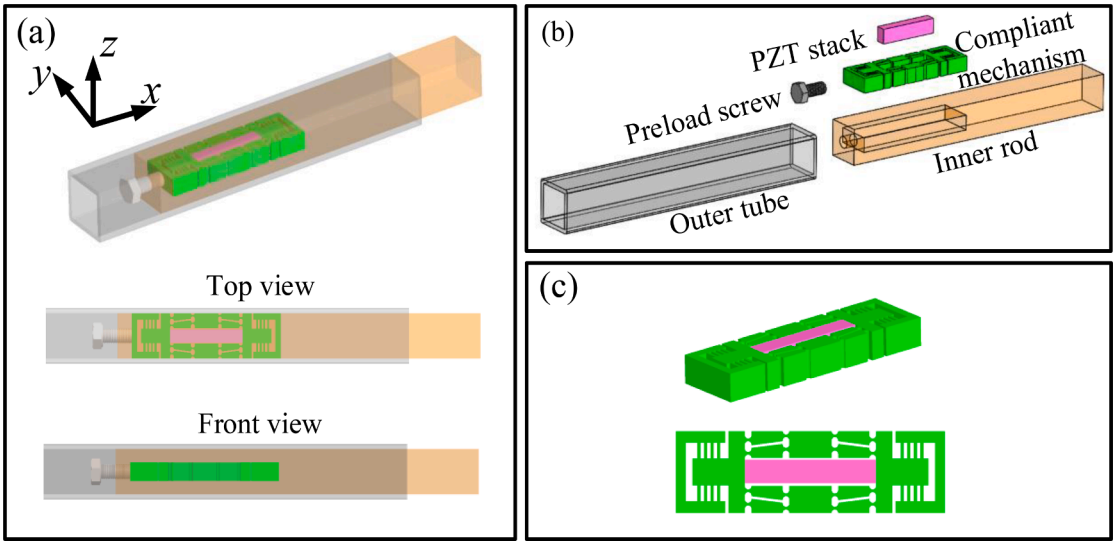

Fig. 2. The CAD model of the lockable joint. (a) Assembled views. (b) Explosion views. (c) The inner CM with PZT actuation.

constraints (the displacement constraints imposed on input and output points). The model is obtained using a compliance matrix method [34]. The coupled influence of the PZT actuation and nonlinear deformation of CMPM on the CBCM was also analyzed, which could be used to predict the locking force generated from preloading and to assess the unlocking ability through the PZT actuation. An optimization framework was also proposed to improve the locking force, taking into account the design space, economical manufacturing precision, PZT actuation for releasing, and the yield strength of the material. The nonlinear FEA and experiments were conducted to verify the feasibility of the design and the accuracy of the proposed model.

The rest of this paper is organized as follows: Section 2 introduces the structure design and working principle of the lockable P joint. Section 3 presents the kinetostatic model of the inner CM and PZT stack actuation. Section 4 presents the characteristic analysis of the mechanism with nonlinear FEA verification. The optimization design framework of the lockable devices is also proposed in this section. An optimum design case is carried out in Section 5 with its nonlinear FEA and experimental verification. Conclusions are drawn in Section 6.

2. System structure and working principle of the lockable P joint

A modular lockable joint can be viewed as a telescopic rod with a locking function. Its design space is mainly focused on the axial direction so that the telescopic rod could be slender and easy to be assembled in a compact space. Thus, we place the PZT actuator horizontally and use a CM to convert the horizontal movement into vertical movement, allowing the inner CM and outer parts to engage and disengage. In general, the design requirements are listed as follows:

- The CM should be able to convert axial movement into strictly lateral contraction when actuation works (no parasitic motion of the output stages along the axial axis).
- The CM should be stiff enough in the axial direction to transmit and bear large loads. Besides, it should allow for millimeter-level deformation in the axial direction to facilitate the adjustment of the preload.
- The device can produce a large locking force (the normal force output by the CM) with a reasonable manufacturing accuracy. This means that the mechanism should have a large output stiffness with a required output displacement.
- The device is capable of quickly switching between the locking and releasing states through smart material actuation.
- The maximum stress in the CM should not exceed the yield strength of the material.

2.1. Structural design and assembly

Fig. 2 illustrates the design and the assembly of the proposed lockable device. There are five parts (Fig. 2(b)), including an outer tube, an inner rod, a CM, a preload screw, and a PZT stack. The PZT stack is installed in the center of the CM (Fig. 2(c)), and the CM is inserted into the through slot of the inner rod (Fig. 2(a)). The preload screw is mounted on the left side of the inner rod. It is capable of fixing the CM and imposing axial (x-direction) pressure force on it.

The inner CM is the key for transmitting motion and force from the axial direction to the lateral direction. The design is based on CBCM with lumped compliance in order to achieve compact space and high output stiffness. In addition, the double-arm in the CBCM will provide motion guidance constraints for the output stage in the lateral direction.

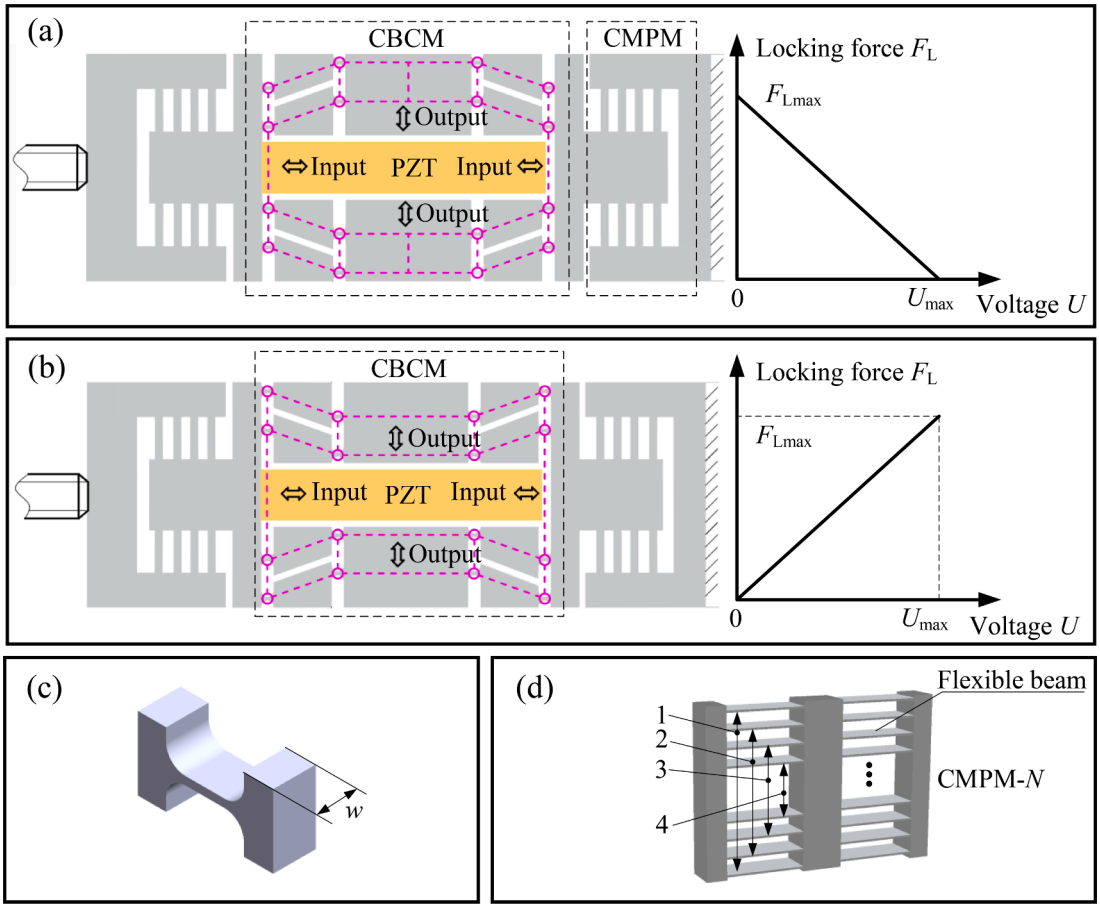

Fig. 3. The designs of two types of locking. (a) Normally locking design. (b)Normally releasing design. (c) A corner-filleted flexure hinge used in the CBCM. (d) A CMPM with $N = 4$.

A pair of symmetrical CMPMs (Fig. 3(d)) are connected at both input sides of the CBCM (Fig. 3(a) and (b)) to ensure that both input sides can produce the same displacements along the x-axis when the PZT is activated. Thus, there will be no parasitic motion of the output stage along the x-axis under the PZT actuation. Besides, a CMPM can produce a high x-direction stiffness without compromising its motion range [35]. Due to this characteristic, we can apply a large axial force to the CM through the preloading screws, and the preloading force is not too sensitive to the moving distance of the screw. More specifically, by measuring the number of turns of the screw, we can approximate the preload force imposed on the CM.

There are two types of locking through using this design concept. The first is the normally locking design (can also be regarded as a self-locking design), as shown in Fig. 3(a). It can be normally locked under the force from the preload screw, allowing energy-free locking. For this type of design, a high locking force is easily achieved since the locking force is determined by the force from the preload screw, rather than by the PZT actuation. Upon applying a voltage to the PZT stack, the joint can be released (The detailed working principle will be given in the next section.). Therefore, it is suitable for systems that lock the shape/pose most of the time, and release the joint to change the shape/pose as required.

Another design is the normally releasing design, as illustrated in Fig. 3(b). Voltage input is required to realize its locking function. Hence, this type of design contributes to temporarily enhancing the stiffness or changing the motion constraints of a system. The following studies focus on the normally locking design considering its benefits in energy consumption, while the other type of design can also be studied similarly using the method presented in this paper.

2.2. *Working principle*

In this section, we explain how the lockable device works. A video animation is also provided in the supplementary materials to demonstrate the principle of the lockable joint, where the CAD model is based on the design case provided in Section 5.

Fig. 4(a) and (b) illustrate the motion of the inner CM before full assembly. As the preload screw compresses the inner CM, the clearance c (labeled in Fig. 4(a)) between the PZT and CBCM disappears while the width of the CBCM increases (Fig. 4(b)).

Fig. 4(c) and (d) show the locking and releasing functions when the device is fully assembled. During preloading, the width of the

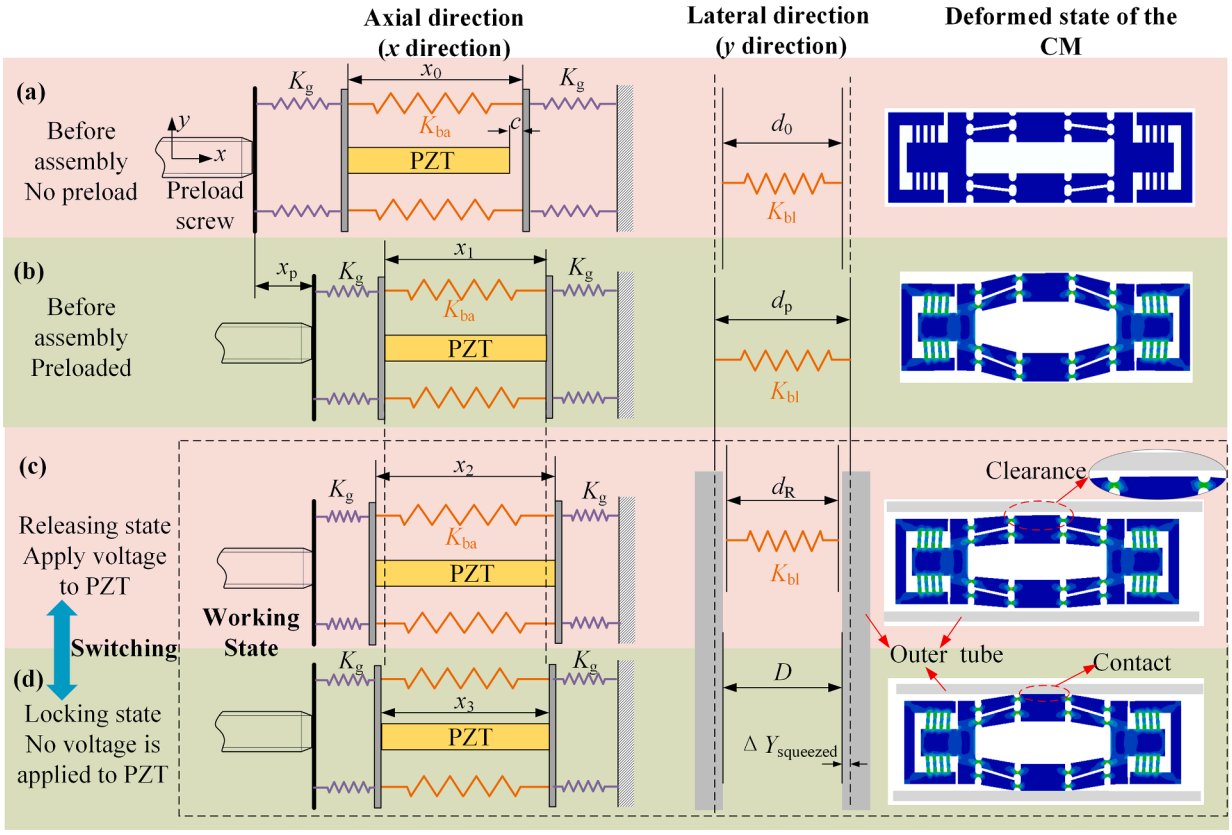

Fig. 4. Working principle of the PZT-compliant-mechanism system.

inner CM (with no output displacement constraints) should be wider than the outer tube's inner diameter (Fig. 4(b)), so as to make the CM be in contact with the outer tube (Fig. 4(d))); When the PZT works, the width of the CM should be smaller than it, as shown in Fig. 4 (c). These relationships can be described as

$$\begin{cases} d_{\mathrm{p}} > D, \text{can generate locking force} \\ d_{\mathrm{R}} < D, \text{releasing} \end{cases} \tag{1}$$

where, d_{p} is the width of the inner CM when preloaded with no output displacement constraints, d_{R} is the width of the inner CM when the PZT is applied with the maximum voltage, and D is the inner diameter of the outer tube, as labeled in Fig. 4(d).

Although the inner CM works on the basis of a simple principle, the design of it requires comprehensive consideration of its motion and stiffness characteristics in both directions, as illustrated in Fig. 4. In the axial direction, the CBCM should allow tens of microns of compression (x_1-x_0) under thousands of newtons of preloading, due to the short motion range of PZT actuation and the large locking force requirement of the device. The CMPM is desired to transmit the large preload force and generate millimeter-level deformation at the same time to facilitate the adjustment of the preload. In the lateral direction, the output displacement (or amplification ratio) and output stiffness of the CBCM should be trade-off to achieve economic manufacturing tolerances as well as high locking forces.

In the following sections, we will present the modeling approaches of these substructures, along with the characteristics analysis and parametric optimization of this device.

3. Static modeling of the substructures

This section presents the static modeling of the inner CM and PZT stack. The compliance matrix method [34,36] is used to establish the kinetostatic model of CBCM since it has a very concise form for complex configurations CMs under small deformation assumptions [37,38]. It is not necessary to perform an inner force analysis with this method. We will present all of the equations regarding the motion and stiffness of the CM under various input and output conditions in an analytical form.

The input side of the CBCM withstands the forces from CMPM deformation and PZT actuation. A nonlinear analytical model [32] is adopted for kinetostatic analysis of the CBCM, due to the large motion range of the CMPM as required. The constitutive equation of PZT actuation under external load is also given in this section.

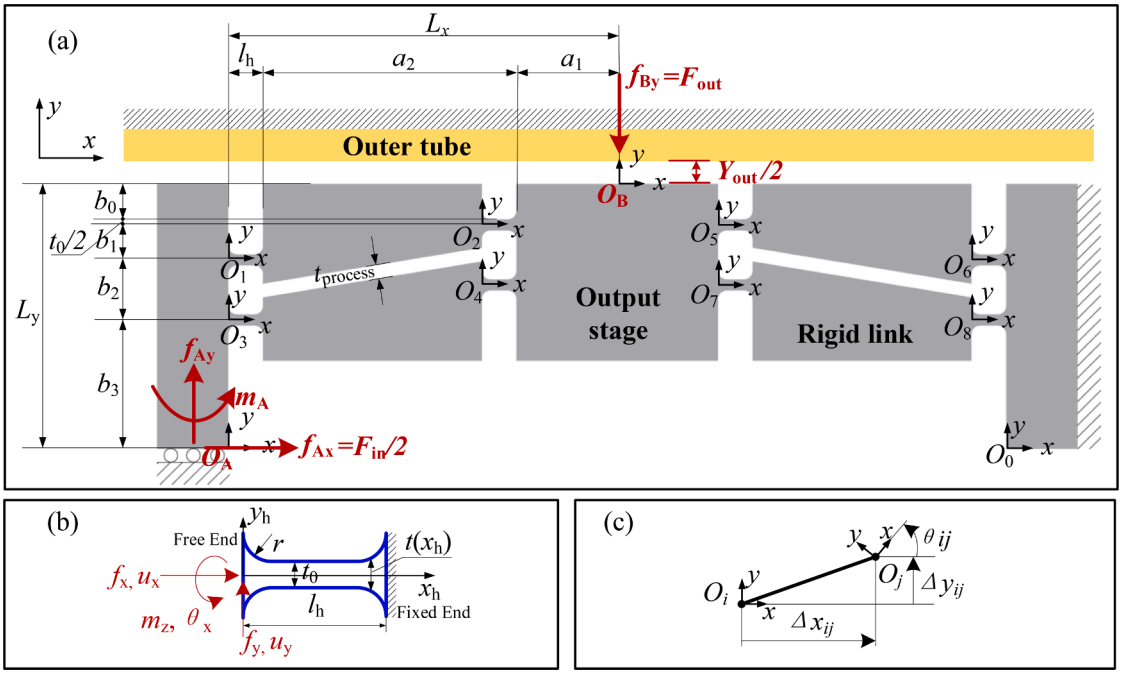

Fig. 5. Statics model and coordinate system of half of the CBCM with output displacement constraints from the outer tube. (a) Key geometry parameters, static force analysis, and coordinate system of the CBCM. (b) Parameters of the conner-filleted hinge. (c) Description of the relative position relationship of the coordinate system.

3.1. Static analysis of the CBCM under input and output displacement constraints

Half of the CBCM is analyzed since the structure of the CBCM is symmetry, as shown in Fig. 5(a). Assuming a flexure hinge (Fig. 5 (b)) has planar 3-DOF deformation, its compliance matrix can be expressed in its local coordinate system as

$$\mathbf{C}_i = \begin{bmatrix} c_{\mathrm{x,F}} & 0 & 0 \\ 0 & c_{\mathrm{y,F}} & c_{\mathrm{y,M}} \\ 0 & c_{\theta,\mathrm{F}} & c_{\theta,\mathrm{M}} \end{bmatrix} \tag{2}$$

where, $c_{\mathrm{x,F}}$, $c_{\mathrm{y,F}}, c_{\mathrm{y,M}}$, $c_{\theta,\mathrm{F}}, c_{\theta,\mathrm{M}}$ are the parameters in the compliance matrix. It describes the relationship between loads and displacements at the free end of a flexure hinge, which can be expressed as $\varepsilon_i = \mathbf{C}_i F_i$, with $\varepsilon_i = [u_{\mathrm{x}}\ u_{\mathrm{y}}\ \theta_{\mathrm{z}}]$, $F_i = [f_{\mathrm{x}}\ x_{\mathrm{y}}\ m_{\mathrm{z}}]$, where u_{x}, u_{y}, θ_{z}, $f_{\mathrm{x}}, f_{\mathrm{y}}$, m_z are labeled in Fig. 5(b).

The compliance parameters in Eq. (2) could be calculated by analytical models [39,40] or empirical formulas [41,42] for various kinds of flexure hinges such as right-circular, conner-filleted, and elliptical. This design chooses the corner-filleted hinge (Fig. 5(b)) because of its lower stress and large deformation ranges [43]. We used the analytical formulas from Ref. [36] to calculate the compliance parameters. These equations are also given in Appendix A.

The compliance matrix of the half of CBCM can be obtained by using the deformation superposition principle, while the compliance matrix of each flexure hinge should be transformed into a unified coordinate system first. The transformation of a compliance matrix from coordinate system O_i to O_j can be written as

$$\mathbf{C}_i^j = \mathbf{T}_i^j \mathbf{C}_i \left(\mathbf{T}_i^j\right)^T, \tag{3}$$

in which the transformation matrix $\mathbf{T}_i^j$ can be calculated as

$$\mathbf{T}_i^j = \mathbf{P}_i^j \left(\mathbf{R}_i^j\right)^T, \tag{4}$$

where, the translation matrix $\mathbf{P}_i^j$ and rotation matrix $\mathbf{R}_i^j$ are defined based on the relative geometric relationship of the two coordinate systems, given as

$$\mathbf{R}_i^j = \begin{bmatrix} \cos\theta_{ij} & \sin\theta_{ij} & 0 \\ -\sin\theta_{ij} & \cos\theta_{ij} & 0 \\ 0 & 0 & 1 \end{bmatrix}, \quad \mathbf{P}_i^j = \begin{bmatrix} 1 & 0 & y_{ij} \\ 0 & 1 & -x_{ij} \\ 0 & 0 & 1 \end{bmatrix}, \tag{5}$$

in which θ_{ij}, x_{ij}, y_{ij} are defined in Fig. 5(c). Note that the displacement offset x_{ij}, y_{ij} is positive when its orientation is consistent with the direction labeled in Fig. 5(c). The rotation matrix $\mathbf{R}_i^j$ becomes a unity matrix when the axes of the two coordinates system are parallel.

The half CBCM has a parallel-serial structure. The compliance of the two parallel structures (O_1 to O_4 and O_5 to O_8) can be first derived as

$$\begin{aligned} \mathbf{C}_{1-4}^2 &= \left[\left[\mathbf{T}_1^2\mathbf{C}_1\left(\mathbf{T}_1^2\right)^{\mathrm{T}} + \mathbf{T}_2^2\mathbf{C}_2\left(\mathbf{T}_2^2\right)^{\mathrm{T}}\right]^{-1} + \left[\mathbf{T}_3^2\mathbf{C}_3\left(\mathbf{T}_3^2\right)^{\mathrm{T}} + \mathbf{T}_4^2\mathbf{C}_4\left(\mathbf{T}_4^2\right)^{\mathrm{T}}\right]^{-1}\right]^{-1}, \\ \mathbf{C}_{5-8}^6 &= \left[\left[\mathbf{T}_5^6\mathbf{C}_5\left(\mathbf{T}_5^6\right)^{\mathrm{T}} + \mathbf{T}_6^6\mathbf{C}_6\left(\mathbf{T}_6^6\right)^{\mathrm{T}}\right]^{-1} + \left[\mathbf{T}_7^6\mathbf{C}_7\left(\mathbf{T}_7^6\right)^{\mathrm{T}} + \mathbf{T}_8^6\mathbf{C}_8\left(\mathbf{T}_8^6\right)^{\mathrm{T}}\right]^{-1}\right]^{-1}, \end{aligned} \tag{6}$$

in which $\mathbf{C}_{1-4}^2$ stands for compliance matrix of the parallel structure O_1 to O_4 in coordinate system O_2, and $\mathbf{C}_{5-8}^6$ stands for the compliance matrix of the parallel structure O_5 to O_8 in coordinate system O_6.

Then, to calculate the motion of the input point O_A (labeled in Fig. 5(a)), the compliance matrices in Eq. (6) are with respect to the coordinate system O_A, which are also labeled as matrices $\boldsymbol{\alpha}$ and $\boldsymbol{\beta}$ in Eq. (7.1). Through linear superposing the displacement at point O_A generated by the forces F_A and F_B from input point O_A and output point O_B respectively, the displacement of the input point ε_A can be derived as

$$\varepsilon_A = \underbrace{\left[\mathbf{T}_2^A\mathbf{C}_{1-4}^2\left(\mathbf{T}_2^A\right)^{\mathrm{T}} + \mathbf{T}_6^A\mathbf{C}_{5-8}^6\left(\mathbf{T}_6^A\right)^{\mathrm{T}}\right]}_{\boldsymbol{\alpha}} F_A + \underbrace{P_B^A\left[\mathbf{T}_6^B\mathbf{C}_{5-8}^6\left(\mathbf{T}_6^B\right)^{\mathrm{T}}\right]}_{\boldsymbol{\beta}} F_B. \tag{7.1}$$

Similarly, the displacement ε_B in the output point O_B generated from F_A and F_B can be derived as

$$\varepsilon_B = \underbrace{P_A^B\left[\mathbf{T}_6^A\mathbf{C}_{5-8}^6\left(\mathbf{T}_6^A\right)^{\mathrm{T}}\right]}_{\boldsymbol{\varepsilon}} F_A + \underbrace{\left[\mathbf{T}_6^B\mathbf{C}_{5-8}^6\left(\mathbf{T}_6^B\right)^{\mathrm{T}}\right]}_{\boldsymbol{\gamma}} F_B, \tag{7.2}$$

where, the displacement vectors $\varepsilon_A, \varepsilon_B$, and force vectors F_A, F_B are given as

$$\begin{aligned} F_A &= \left\{f_{Ax}\ f_{Ay}\ m_A\right\}^{\mathrm{T}} \\ F_B &= \left\{0\ -f_{By}\ 0\right\}^{\mathrm{T}} \\ \varepsilon_A &= \left\{x_A\ 0\ 0\right\}^{\mathrm{T}} \\ \varepsilon_B &= \left\{x_B\ y_B\ \theta_B\right\}^{\mathrm{T}}. \end{aligned} \tag{8}$$

The two unknown reaction forces at O_A, f_{Ay} and m_A, can be determined by solving the second and third equations in Eq. (7.1), which are given as

$$\begin{aligned} f_{Ay} &= \frac{(\alpha_{21}\alpha_{33} - \alpha_{31}\alpha_{23})f_{Ax} + (\alpha_{33}\beta_{22} - \alpha_{23}\beta_{32})\left(-f_{By}\right)}{\alpha_{23}\alpha_{32} - \alpha_{22}\alpha_{33}}, \\ m_A &= \frac{(\alpha_{21}\alpha_{32} - \alpha_{31}\alpha_{22})f_{Ax} + (\alpha_{32}\beta_{22} - \alpha_{22}\beta_{32})\left(-f_{By}\right)}{\alpha_{22}\alpha_{33} - \alpha_{23}\alpha_{32}}. \end{aligned} \tag{9}$$

where, α_{ij} or β_{ij} ($i, j = 1, 2, 3$) are the ith row and jth column of the matrix $\boldsymbol{\alpha}$ or $\boldsymbol{\beta}$ from Eq. (7.1).

Then, substituting Eq. (9) to the first equation in Eq. (7.1) and the second equation in Eq. (7.2), the displacements at points O_A and O_B can be derived as

$$\begin{aligned} x_A &= \alpha_{11}f_{Ax} + \alpha_{12}f_{Ay} + \alpha_{13}m_A + \beta_{12}\left(-f_{By}\right) \\ &= \left(\alpha_{11} + \alpha_{12}\frac{\alpha_{21}\alpha_{33} - \alpha_{31}\alpha_{23}}{\alpha_{23}\alpha_{32} - \alpha_{22}\alpha_{33}} + \alpha_{13}\frac{\alpha_{21}\alpha_{32} - \alpha_{31}\alpha_{22}}{\alpha_{22}\alpha_{33} - \alpha_{23}\alpha_{32}}\right)f_{Ax} - \left(\beta_{12} + \alpha_{12}\frac{\alpha_{33}\beta_{22} - \alpha_{23}\beta_{32}}{\alpha_{23}\alpha_{32} - \alpha_{22}\alpha_{33}} + \alpha_{13}\frac{\alpha_{32}\beta_{22} - \alpha_{22}\beta_{32}}{\alpha_{22}\alpha_{33} - \alpha_{23}\alpha_{32}}\right)f_{By} \\ y_B &= \varepsilon_{21}f_{Ax} + \varepsilon_{22}f_{Ay} + \varepsilon_{23}m_A + \gamma_{22}\left(-f_{By}\right) \\ &= \left(\varepsilon_{21} + \varepsilon_{22}\frac{\alpha_{21}\alpha_{33} - \alpha_{31}\alpha_{23}}{\alpha_{23}\alpha_{32} - \alpha_{22}\alpha_{33}} + \varepsilon_{23}\frac{\alpha_{21}\alpha_{32} - \alpha_{31}\alpha_{22}}{\alpha_{22}\alpha_{33} - \alpha_{23}\alpha_{32}}\right)f_{Ax} - \left(\gamma_{22} + \varepsilon_{22}\frac{\alpha_{33}\beta_{22} - \alpha_{23}\beta_{32}}{\alpha_{23}\alpha_{32} - \alpha_{22}\alpha_{33}} + \varepsilon_{23}\frac{\alpha_{32}\beta_{22} - \alpha_{22}\beta_{32}}{\alpha_{22}\alpha_{33} - \alpha_{23}\alpha_{32}}\right)f_{By}. \end{aligned} \tag{10}$$

where, ε_{ij} or γ_{ij} ($i, j = 1, 2, 3$) are the ith row and jth column of the matrix $\boldsymbol{\varepsilon}$ or $\boldsymbol{\gamma}$ from Eq. (7.2).

Eq. (10) can be rewritten in a more concise form, given as

$$\begin{pmatrix} x_A \\ y_B \end{pmatrix} = \begin{bmatrix} c_{11} & c_{12} \\ c_{21} & c_{22} \end{bmatrix} \cdot \begin{pmatrix} f_{Ax} \\ f_{By} \end{pmatrix} \tag{11}$$

in which the parameters in the compliance matrix of a half CBCM are

$$\begin{aligned} c_{11} &= \left(\alpha_{11} + \alpha_{12}\frac{\alpha_{21}\alpha_{33} - \alpha_{31}\alpha_{23}}{\alpha_{23}\alpha_{32} - \alpha_{22}\alpha_{33}} + \alpha_{13}\frac{\alpha_{21}\alpha_{32} - \alpha_{31}\alpha_{22}}{\alpha_{22}\alpha_{33} - \alpha_{23}\alpha_{32}}\right) \\ c_{12} &= -\left(\beta_{12} + \alpha_{12}\frac{\alpha_{33}\beta_{22} - \alpha_{23}\beta_{32}}{\alpha_{23}\alpha_{32} - \alpha_{22}\alpha_{33}} + \alpha_{13}\frac{\alpha_{32}\beta_{22} - \alpha_{22}\beta_{32}}{\alpha_{22}\alpha_{33} - \alpha_{23}\alpha_{32}}\right) \\ c_{21} &= \left(\varepsilon_{21} + \varepsilon_{22}\frac{\alpha_{21}\alpha_{33} - \alpha_{31}\alpha_{23}}{\alpha_{23}\alpha_{32} - \alpha_{22}\alpha_{33}} + \varepsilon_{23}\frac{\alpha_{21}\alpha_{32} - \alpha_{31}\alpha_{22}}{\alpha_{22}\alpha_{33} - \alpha_{23}\alpha_{32}}\right) \\ c_{22} &= -\left(\gamma_{22} + \varepsilon_{22}\frac{\alpha_{33}\beta_{22} - \alpha_{23}\beta_{32}}{\alpha_{23}\alpha_{32} - \alpha_{22}\alpha_{33}} + \varepsilon_{23}\frac{\alpha_{32}\beta_{22} - \alpha_{22}\beta_{32}}{\alpha_{22}\alpha_{33} - \alpha_{23}\alpha_{32}}\right). \end{aligned} \tag{12}$$

To obtain the compliance matrix of the whole mechanism, the force and displacement relationships between the half and the whole CBCM are established, given as

$$f_{Ax} = \frac{F_{in}}{2}, f_{By} = F_{out}, y_B = \frac{Y_{out}}{2},\ x_A = X_{in} \tag{13}$$

where, F_{in}, F_{out}, X_{in}, Y_{out} stands for input-output force and displacement of the whole CBCM, respectively. Using Eqs. (11) and (13), the constitutive equations of the whole CBCM describing the relationship between the input-output displacements and forces can be derived as

$$\begin{pmatrix} X_{in} \\ Y_{out} \end{pmatrix} = \mathbf{C}\begin{pmatrix} F_{in} \\ F_{out} \end{pmatrix} = \begin{bmatrix} \frac{1}{2}c_{11} & c_{12} \\ c_{21} & 2c_{22} \end{bmatrix} \begin{pmatrix} F_{in} \\ F_{out} \end{pmatrix} \tag{14}$$

where, $\mathbf{C}$ is the compliance matrix of the whole CBCM, and its inverse matrix $\mathbf{K}$ is the stiffness matrix of the CM, i.e., $\mathbf{K} = \mathbf{C}^{-1}$.

Using Eq. (14), the static characteristics of the CBCM under various load/displacement conditions can be obtained. We mainly focus on calculating the required input actuation force and the output normal contact force with given input and output displacement constraints. However, a brief discussion of the static characteristics with different load/displacement conditions of CBCM will be presented here, since it could be used to analyze the static characteristics of the mechanism before and after contact with other objects, as well as facilitate readers to use these equations for different applications. Four cases are investigated as follows:

(1)If the mechanism has input and output displacement constraints (X_{in} and X_{out}), through solving Eq. (14), its input and output force can be derived as

$$F_{in} = \frac{2c_{22}X_{in} - c_{12}Y_{out}}{c_{22}c_{11} - c_{12}c_{21}} \tag{15}$$

$$F_{out} = \frac{2c_{21}X_{in} - c_{11}Y_{out}}{2c_{12}c_{21} - 2c_{11}c_{22}} \tag{16}$$

Then the motion and force transmission property (A_c and A_f) can be expressed as ((A_f)$^{-1}$ is given since it is easier to compare the motion amplification and force reduction ratios of the mechanism)

$$\begin{aligned} A_c &= \frac{Y_{out}}{X_{in}} \\ (A_f)^{-1} &= \frac{F_{in}}{F_{out}} = -\frac{4c_{22}X_{in} - 2c_{12}Y_{out}}{2c_{21}X_{in} - c_{11}Y_{out}} \end{aligned} \tag{17}$$

This case can be used to analyze the static characteristics after the CBCM contact with the outer tube.

(2)If the mechanism just has input displacement constraints (X_{in}) with no output forces, substitute F_{out}=0 to Eq. (16), then solve Eqs. (15) and (16) for the input force and output displacement, given as

$$F_{in} = \frac{2}{c_{11}}X_{in} \tag{18}$$

$$Y_{out} = 2\frac{c_{21}}{c_{11}}X_{in} \tag{19}$$

The motion and force transmission properties (A_c and A_f) are derived as

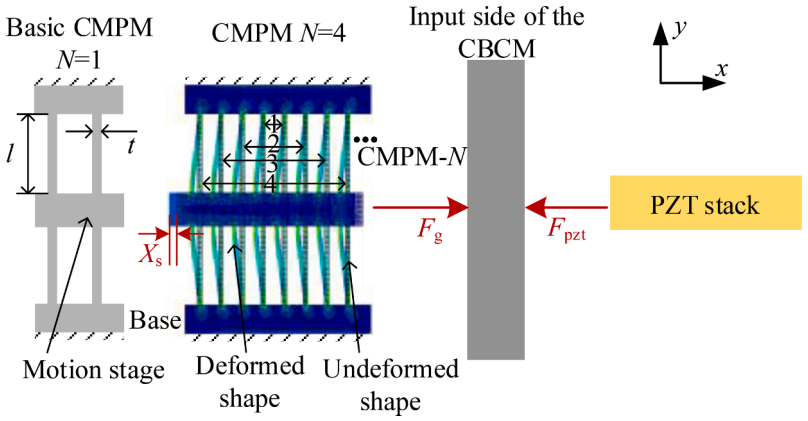

Fig. 6. Input forces on the CBCM from the CMPM and the PZT stack.

$$A_c = \frac{Y_{out}}{X_{in}} = 2\frac{c_{21}}{c_{11}}$$
$$A_f = \frac{F_{out}}{F_{in}} = 0 \tag{20}$$

This case can be used to analyze the static characteristics before the CBCM contact with the outer tube.

(3)If the mechanism just has the output displacement constraints (X_{out}) with no input forces, substitute F_{in}=0 to Eq. (15), then solve it for the output force and input displacement, given as

$$F_{out} = \frac{1}{2c_{22}}Y_{out} \tag{21}$$

$$X_{in} = \frac{c_{12}}{2c_{22}}Y_{out} \tag{22}$$

Then the motion and force transmission properties (A_c and A_f) are derived as

$$A_c = \frac{Y_{out}}{X_{in}} = 2\frac{c_{21}}{c_{11}}$$
$$A_f = \frac{F_{out}}{F_{in}} = 0 \tag{23}$$

In the next section, we will use this case to analyze the output stiffness with no input constraints and compare it with the case that has input and output displacement constraints.

(4)If the mechanism has input and output forces constraints (F_{in} and F_{out}), Eq. (14) can be directly used to calculate the input and output displacement. The motion and force transmission properties can be derived as

$$A_c = \frac{X_{out}}{X_{in}} = \frac{2c_{12}F_{in} + 4c_{22}F_{out}}{c_{11}F_{in} + 2c_{12}F_{out}}$$
$$A_f = \frac{F_{out}}{F_{in}} \tag{24}$$

This case can be used to evaluate the motion transmission property when force constraints exist.

3.2. Static modeling of the CMPM and PZT stack

When we analyze the static characteristics of the whole system, the influence of the CMPM and the PZT actuation should be taken into count. As shown in Fig. 6, the input force (F_{in}) on the CBCM equals the superposition of axial deformation force (F_g) from CMPM and the force from the PZT stack (F_{pzt}), which can be written as

$$F_{in} = F_g - F_{pzt} \tag{25}$$

The static equations that describe the relationship between the axial displacement and load of CMPM-*N* from [32] can be represented as

$$F_g = N\frac{EIX_s}{l^3}\left(48 + 1.2\left(\frac{2.4X_s^2}{t^2/12 + X_s^2/700}\right)\right) \tag{26}$$

Table 1
Geometry and mechanical parameters of the CBCMs.

	a_1	a_2	b_0	b_1	b_2	b_3	l_h	t_0	r	L_x	L_y
Case 1	9	16	2	1	4	10	5	1	0.5	30	15
Case 2	4	26	2	2.2	7.6	7.6	5	1.2	1.5	35	20
Material Al 7075-T651 E= 71 Gpa Poisson's ratio $\gamma = 0.33$ [σ]= 500 Mpa											

where, $I = wt^3/12$ is the area moment of inertia of the beam cross-section, N is the number of the basic CMPM groups, E is Young's modulus of the material, F_g is the axial force from the guiding mechanism (CMPM) imposing on the CBCM, X_s is the axial direction displacement of the motion stage with respect to the base of CMPM, l, t, and w are the length, thickness, and the out of plane width of the flexible beam, respectively, as labeled in Fig. 6.

For the PZT actuation, when voltage V is applied to it, its output force and output displacement [44] has the following relationship

$$F_{pzt} = \left(\frac{L_0}{V_{max}} V - \delta_{pzt}\right) k_{pzt}, \tag{27}$$

where, L_0 is the free expansion of the PZT stack when the maximum voltage V_{max} is applied to it, δ_{pzt} is the output displacement of the PZT stack. The stiffness of the PZT stack k_{pzt} in Eq.(27) can be evaluated as

$$k_{pzt} = \frac{E^* A}{L_{pzt}}, \tag{28}$$

in which E^* is the effective modulus of elasticity of the piezoceramic material, A and L_{pzt} are the cross-sectional area and the length of the PZT actuator, respectively.

4. Characteristics and optimization

This section analyses the static characteristics of the mechanism for locking applications and is verified by FEA. Besides, an optimization framework is also provided to optimize the geometry parameters of the CM to improve the locking force considering the design space, economical manufacturing precision, PZT actuation for releasing, and the yield strength of the material.

4.1. Static characteristics of the inner CBCM

Two design cases with different dimensions are used to investigate the static characteristics of the CBCM for locking applications. The geometry and mechanical parameters of the two design cases are given in Table 1. When the input displacement is given, the output normal contact force and the required input force can be calculated by Eqs. (15) and (16). Before contact, the input force and output displacement can be calculated by Eqs. (18) and (19). In the simulation, the maximum input displacement of the CBCM is set as 40 μm, given the small output displacement of the PZT actuation. Different clearances between the CBCM and the outer tube are investigated, which are set as c_1=D-d_0 = 0, 0.02, 0.04 mm, respectively, where D and d_0 are labeled in Fig. 4.

Fig. 7 shows the simulated results using the analytical model presented in Section 3.1 as well as the FEA. The Young's modulus E in the analytical model simulation was modified by $E' = E/(1-\gamma^2)$, considering that a relatively large z-direction dimension in a short beam will result in the plane strain in XY plane deformation.

The FEA-based simulation was performed based on ANSYS Workbench 2020. The simulation set the links, input/output stages and outer tube as rigid. Hex domain mesh division was adopted and the finer mesh was generated in the flexure hinges. Through imposing the displacement constraints on the input and output sides of CBCM, the required input force and normal contact force can be obtained by using "force reaction" in the "contact tool". From the results of the two cases given in Fig. 7, it can be observed that:

1) The present model could accurately evaluate the static performance of the CBCM under both sides' displacement constraints. Compared with FEA results, the analytical model has an average percentage error of 3∼ ∼ 4% in predicting the required input force (Fig. 7(a), (c) and (e)), and an average percentage error of 2∼ ∼ 3% in predicting the normal contact force (Fig. 7(b), (g) and (h)). These errors mainly come from the uncertainty of the compliance matrix of the flexure hinge and the inherent difference between the FEA model and the analytical model.
2) The input stiffness k_{in} of the CMs (*slopes* in Fig. 7(a), (c) (d) (e) and (f)) are abruptly enhanced after the contact occurs. Before contact, the input stiffness of case 1 is 4.24×10^4 N/mm, and case 2 is 2.47×10^4 N/mm. After contact, the input stiffness of case 1 increases to 1.48×10^5 N/mm, and that of case 2 increases to 2.10×10^5 N/mm, increasing by 3.5 and 8.5 times, respectively. The output stiffness k_{out} (*slopes/amplification ratio* in Fig. 7(b), (g) and (h)) with input displacement constraints is also enhanced compared with cases with no input displacement constraints. According to Eq. (21), the output stiffness with no input displacement constraints can be calculated as $1/(2c_{22})$ and the specific values for the two cases are 214.23 N/mm and 196.20 N/mm, respectively. If the mechanisms have input displacement constraints, the stiffness will be changed to 746.84 N/mm and 1669.75 N/mm, increasing by 3.5 and 8.5 times compared with the cases with no input displacement constraints. A large output stiffness is beneficial to the locking applications since a small contact distance can generate a large locking force.

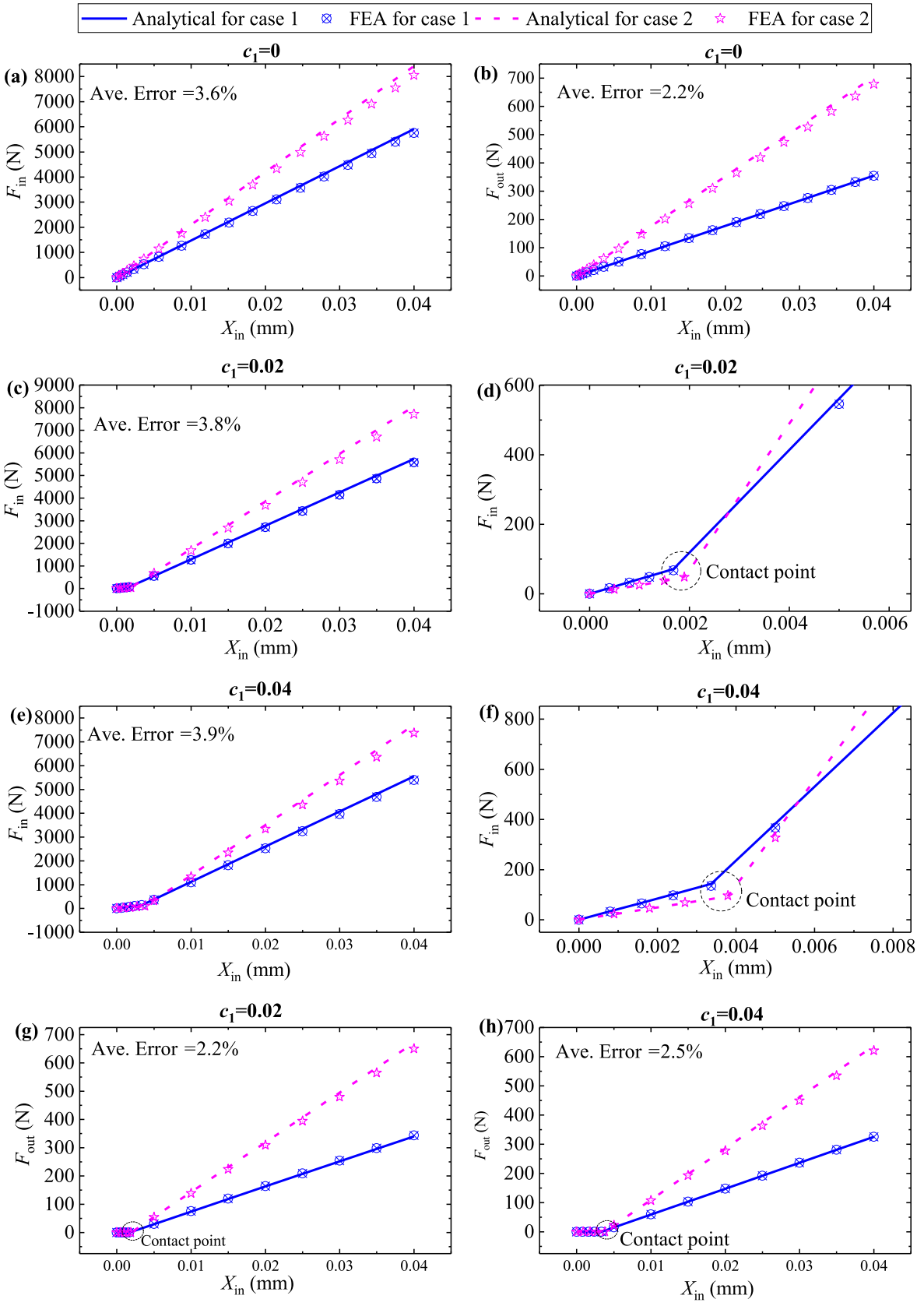

(caption on next page)

Fig. 7. Input and output force calculation results with input and output displacement constraints. (a) Input force for clearance $c_1 = 0$. (b) Output force for $c_1 = 0$. (c) Input force for $c_1 = 0.02$ mm. (d) Partial enlarged view of Fig. 7(c) ranges $X_{in} \in [0, 0.005]$ mm. (e) Input force for $c_1 = 0.04$ mm. (f) Partial enlarged view of Fig. 7(e) ranges $X_{in} \in [0, 0.008]$ mm. (g) Output force for clearance $c_1 = 0.02$ mm. (h) Output force for clearance $c_1 = 0.04$ mm.

3) The smaller the clearance, the larger the locking force. According to the results of the analytical model simulation, when the maximum input distance 40 μm is reached, the maximum output force (F_{out}) of design case 1 can be achieved 354.45, 339.84, 324.90 N with the clearance c_1 set as 0, 0.02, 0.04 mm, respectively. For the second design case, the maximum output force can achieve 704.20, 670.80, 637.41 N with clearance c_1 set as 0, 0.02, 0.04 mm, respectively.
Since there are two contact surfaces for the proposed design, the corresponding locking force can be calculated as $F_L = 2\mu_1 F_{out}$, where μ_1 is the coefficient of friction between the inner CBCM and outer tube. The frictional coefficient for some common materials can be found in [45], in which the coefficient of the dry Al-Al is 1.05, and the coefficient of dry mild-steel-mild-steel is 0.74. A simple inclined plane experiment can also calibrate this coefficient.
If we set $\mu_1 = 0.8$, and $c_1 = 0.02$, in theory, the two cases can achieve 543.74 N and 1073.28 N locking force, respectively. Hence, the present design can generate a large locking force, which is related to the dimension of CBCM, the frictional coefficients, and fit clearance. A smaller fit clearance will generate a larger locking force but will present machining challenges and is uneconomical. The optimization design model present in the later section will take these points into count.

The motion and force transmission properties are also investigated for the two design cases. Using Eqs. (17) and (20), the motion amplification ratio with no output displacement constraints (A_c) and the force reduction ratio with both sides' constraints (A_f^{-1}) can be obtained. Fig. 8 plots the force transmission property from the analytical model and FEA model. From these results, we can find that:

The motion amplification ratio (A_c) is relatively smaller than the force reduction ratio (A_f^{-1}), which is different from that of rigid-body mechanisms. For case 1, A_c is 11.88 with an error of 4.9% compared with the FEA results (A_c from FEA is 12.5). A_f^{-1} is around 16.69 with an error of 3.6 % compared with the FEA results (Fig. 8(a)). For case 2, A_c is 10.54 with an error of 6.4% compared with the FEA results ((A_c from FEA is 9.90)). A_f^{-1} is around 12.09 with an error of 1.9 % compared with the FEA results (Fig. 8(b)).

This phenomenon is because the deformation of the compliant hinge consumes a part of energy. Though the use of flexure hinges will reduce the efficiency of force transmission, it can significantly reduce assembly complexity, and the mechanism can be easily scaled down and scaled up.

Note that in Fig. 8, A_f^{-1} just shown the data after contact since F_{out} equals 0 before contact, which means A_f^{-1} is infinite and meaningless. If the CBCM just contacts the outer tube, A_f^{-1} will be very large. This situation can be observed from several points with small input displacement in Fig. 8. Because in these cases, there will be a certain input force due to the deformation before contact, but the output force is very small when just contact. Besides, A_f^{-1} will decrease as input distance increases and approach a fixed value (Fig. 8). It can be explained using Eq. (17) that if we fixed the value of Y_{out}, as X_{in} increases, A_f^{-1} will approach $2c_{22}/c_{21}$.

4.2. Static characteristics of the inner CMPM

A design case is used to illustrate the force-displacement relationship of the inner CMPM. The parameters of the design case are given in Table 2. The range of the displacement is set as 0 ~ 0.5 mm, and the corresponding axial force can be calculated by Eq. (26).

Fig. 9 shows the results from the analytical model and FEA. It is shown that the analytical model can be used to predict the force-displacement relationship of the CMPM, with an average error of 2.8% compared with the FEA results. If we want to use the CMPM to

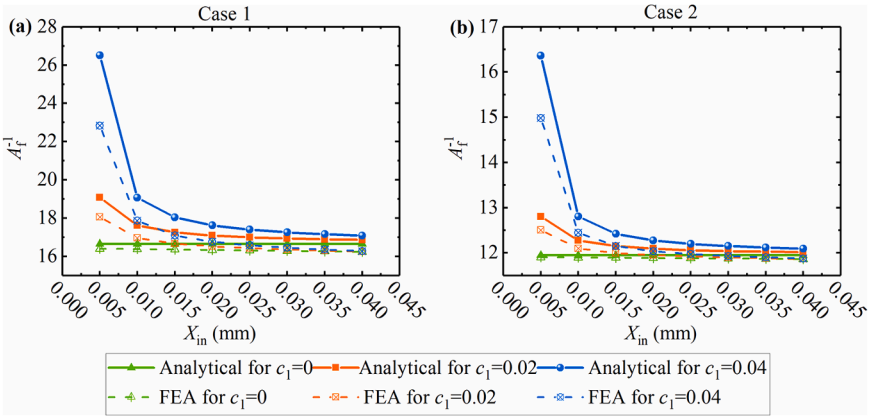

Fig. 8. The force transmission property of the CBCM under both sides' motion constraints. (a) A_f^{-1} for case 1 (b) A_f^{-1} for case 2.

Table 2
Geometry and mechanical parameters of the CMPM.

t	l	w	N	Material
1 mm	14 mm	10 mm	1, 2, 3, 4	Al 7075 T651

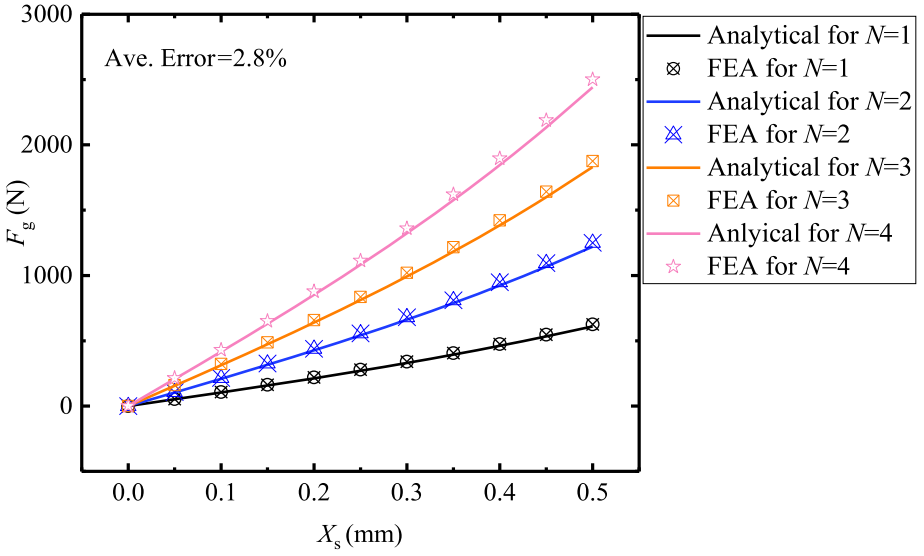

Fig. 9. The force-displacement relationship of a CMPM.

transmit very large axial forces without decreasing the motion range of the CMPM, increasing the group number N gives good results.

However, the motion range is determined by the geometry parameters of a basic CMPM group, which is constrained by the yield strength of the material. In the next section, the proposed optimization model will optimize the group number N and the thickness of the flexible beams in the CMPM, to ensure that the CMPM can transmit the required preload force with a specific deformation range.

4.3. Optimization of the inner CM

A two-step optimization framework is presented in this section to optimize the parameters of the inner CM for locking applications, as illustrated in Fig. 10. The first step is to optimize the design parameters of the CBCM. The target is to obtain the optimal geometry parameters of the CBCM given the overall size of the mechanism, the input driving force and input displacement constraints, which leads to a mechanism with the maximum output force (Eq. (16)) and economic machining accuracy.

The optimization model for CBCM can be written as

$$\tau = \underset{\{a_1,b_0,b_1,b_2,t_0,l_h\}}{\operatorname{argmax}} F_{out} = \frac{2c_{21}X_{in} - c_{11}Y_{out}}{2c_{12}c_{21} - 2c_{11}c_{22}} \tag{29.a}$$

subject to

$$A_c X_{in} - Y_{out} \geq \Delta Y_{squeezed} \tag{29.b}$$

$$F_{in} \leq F_{in\_max} \tag{29.c}$$

$$\begin{aligned} &a_2 = L_x - a_1 - 2r, b_3 = L_y - b_1 - b_2 - \frac{t_0}{2} - r \\ &b_1 \geq 0, b_2 \geq t_0 + 2r + t_{process}, b_3 \geq \frac{t_0}{2} + b_0 + \frac{w_{pzt}}{2}, a_2 \geq 2l_h \end{aligned} \tag{29.d}$$

$$\sigma_{max1} < [\sigma] \tag{29.e}$$

$$a_1 \in [a_{1min}, \quad a_{1max}], b_0 \in [b_{0min}, \quad b_{0max}], l_h \in [l_{hmin}, \quad l_{hmax}], t_0 \in [t_{0min}, \quad t_{0max}] \tag{29.f}$$

in which $\Delta Y_{squeezed}$ stands for the required minimum contact distance of the output side (as labeled in Fig. 4), $t_{process}$ stands for the minimum machining distance between two rigid links (as labeled in Fig. 5), w_{pzt} is the width of the PZT stack.

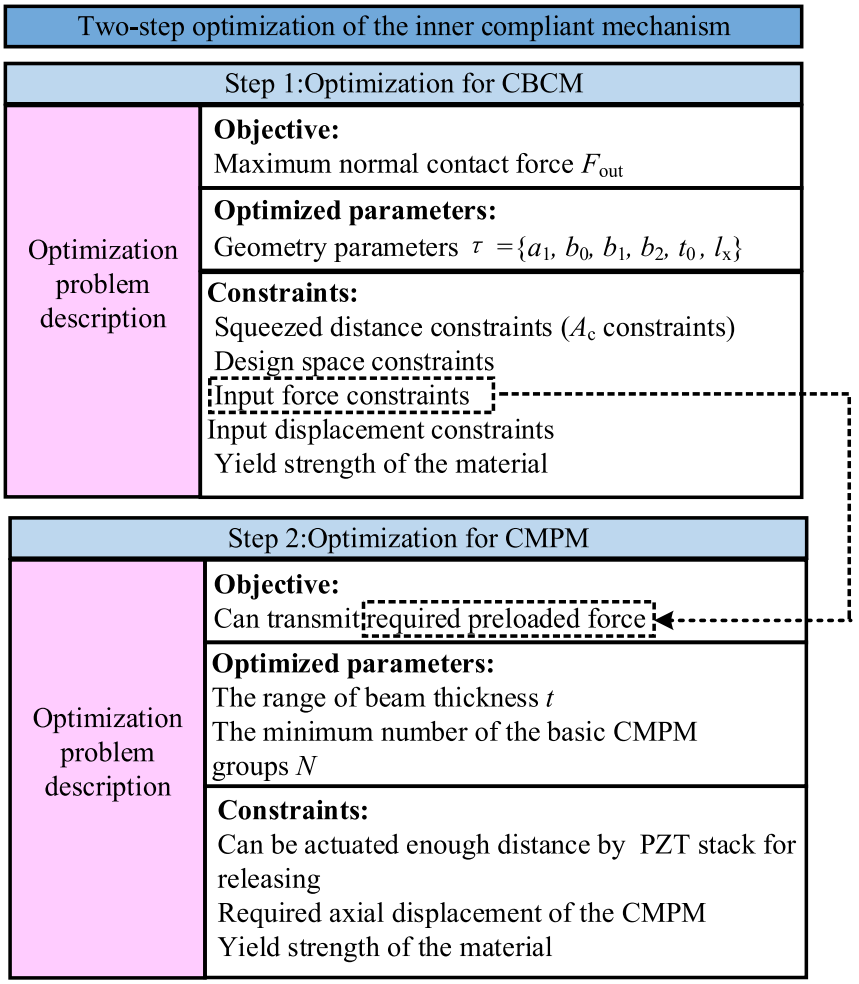

Fig. 10. The framework of the two-step optimization for the inner CM.

The amplification ratio constraint in Eq. (29.a) means that for a given input displacement X_{in}, the output motion ($A_c X_{in}$) could cover the clearance ($Y_{out}=c_1$) and have sufficient contact distance ($\Delta Y_{squeezed}$). The clearance c_1 is equal to the maximum clearance between the inner CM and the outer tube, which is determined by the tolerances of these two parts. Considering the economy of processing accuracy, we can select a preferred fit and tolerance grades from the Standard of Tolerance and Fits (such as Standard GB/T 1801-2009). X_{in} can be evaluated by the performance of a PZT stack.

The input force constraint (Eq. (29.c)) is used to constrain the maximum input force (F_{in_max}) from the CMPM to facilitate the joint release by the PZT stack. Though a PZT stack can generate a high output force, excessive external load or stiffness will decrease its output distance. In the following simulation, we set F_{in_max} as approximately half of the blocking force of the PZT stack. The F_{in_max} can also be used to calculate the required transmission force of the CMPM from preloading, which could serve as a design objective in the next optimization step, as the dashed line shown in Fig. 10.

The design space constraint equations Eq. (29.d) give the overall size constraints of the inner CM and describe the length and relative position constraints of the flexible hinges. Besides, the minimum machining distance $t_{process}$ also takes the machining method into count. For CNC, $t_{process}$ mainly depends on the minimum tool radius. For wire electrical discharge machining, it could be very small, just a little bit larger than the diameter of the wire.

The last constraint Eq. (29.e) comes from the yield strength of the material. Since the mechanism has a symmetry and parallel design, the deformation of all the flexible hinges and limbs are the same. The displacement and bending angle (x_h, y_h, θ_h) of the free end of the hinge can be estimated by the knowing motion constraints of the input and output stages (The derivations are given in Appendix B). Then, the maximum normal stress on the cross-section of the corner-filleted flexure hinges can be calculated as [43]

$$\sigma_{max\,1} = 6k_b/\left(wt_0^2\right)[k_{11} + lk_{12}]\theta_h + (k_{12} + lk_{22})y_h] + k_t/(wt_0)k_{33}x_h \tag{30}$$

in which k_b and k_t are the stress concentration factors in bending and tension, respectively, and k_{11}, k_{12}, k_{22}, k_{33} are the parameters in the stiffness matrix of the flexure hinge. Those parameters have the following relationship (Eq. (31)) with the compliance parameters

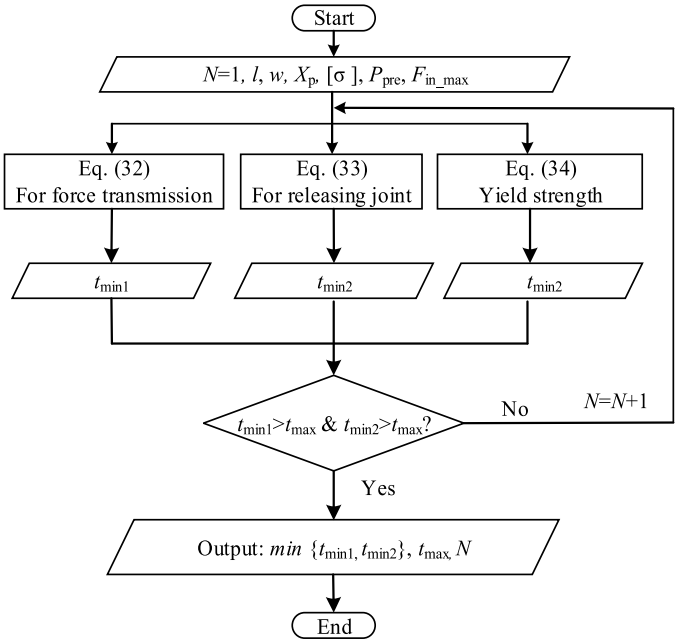

Fig. 11. The Optimization process for the CMPM.

given in Eq. (2). The parameters k_b and k_t can be calculated by using the formulas in [46–48] for various kinds of flexure hinges. We adopted the empirical equations in [48] for circular-conner-filleted flexure hinges in this study. These equations are also given in Appendix C.

$$\begin{cases} k_{11} = c_{y,M} \Big/ \left(c_{\theta,F} c_{y,M} - c_{y,F}^2 \right) \\ k_{12} = -c_{y,F} \Big/ \left(c_{\theta,F} c_{y,M} - c_{\theta,M}^2 \right) \\ k_{22} = c_{\theta,F} \Big/ \left(c_{\theta,F} c_{y,F} - c_{y,F}^2 \right) \\ k_{33} = 1 / c_{x,F} \end{cases} \tag{31}$$

As shown in Fig. 10, the second-step optimization is aimed to determine the thickness (t) of the flexible beams as well as the minimum number of the basic CMPM groups (N). The main design objective of the CMPM is that it could transmit the required preloading force with the required motion range, which can be described as

$$F_{g1} - \left(F_{in\_max} + P_{pre} A \right) \geq 0 \tag{32}$$

where, F_{g1} is the force from CMPM when it has displacement $X_p/2$, A is the cross-section area of the PZT stack, P_{pre} is the required preload pressure on PZT, which is relatively small for non-high-dynamic applications.

If the preload screw moves the distance X_p, each CMPM will generate the same amount of deformation. Hence, F_{g1} can be calculated by substituting $X_s = X_p/2$ into Eq. (26). Note that, in Eq. (32), the squeezed distance of the CBCM is neglected since its deformation is very small compared with the deformation range of CMPM, as mentioned in Section 2. F_{in_max} could use the data in the input force constraints for CBCM in the first step optimization, as the dashed line shown in Fig. 10.

In the preloading process, the CMPM deforms and exerts a force on the CBCM. To release the joint, the PZT should be able to generate enough displacement under the loads from CMPM. In other words, when the PZT produces the displacement we need, its maximum output force ($F_{pzt-max}$) should be larger than or equal to the force from the CMPM (F_{g2}). The maximum output force of the PZT stack under a certain output distance (δ_1) can be obtained by substituting $V = V_{max}$ into Eq. (27), given as $F_{pzt-max} = (L_0 - \delta_1) k_{pzt}$. Hence, the relationship that needs to be satisfied for releasing the joint can be written as

$$F_{pzt\_max} \geq F_{g2} \rightarrow (L_0 - \delta_1) k_{pzt} - F_{g2} \geq 0 \tag{33}$$

in which $\delta_1 = c$ is the required actuation distance for releasing. The parameter c is the initial gap between the PZT stack and CBCM. It equals the required input distance of CBCM X_{in}, which is a known parameter in the optimization model. F_{g2} is the force from CBCM when the joint is released. It can be calculated by substituting $X_s = (X_p + c)/2$ into Eq. (26). Note that when the PZT outputs displacement c, the CBCM will recover its shape before preloading so that the joint could be released, where the axial deformation of

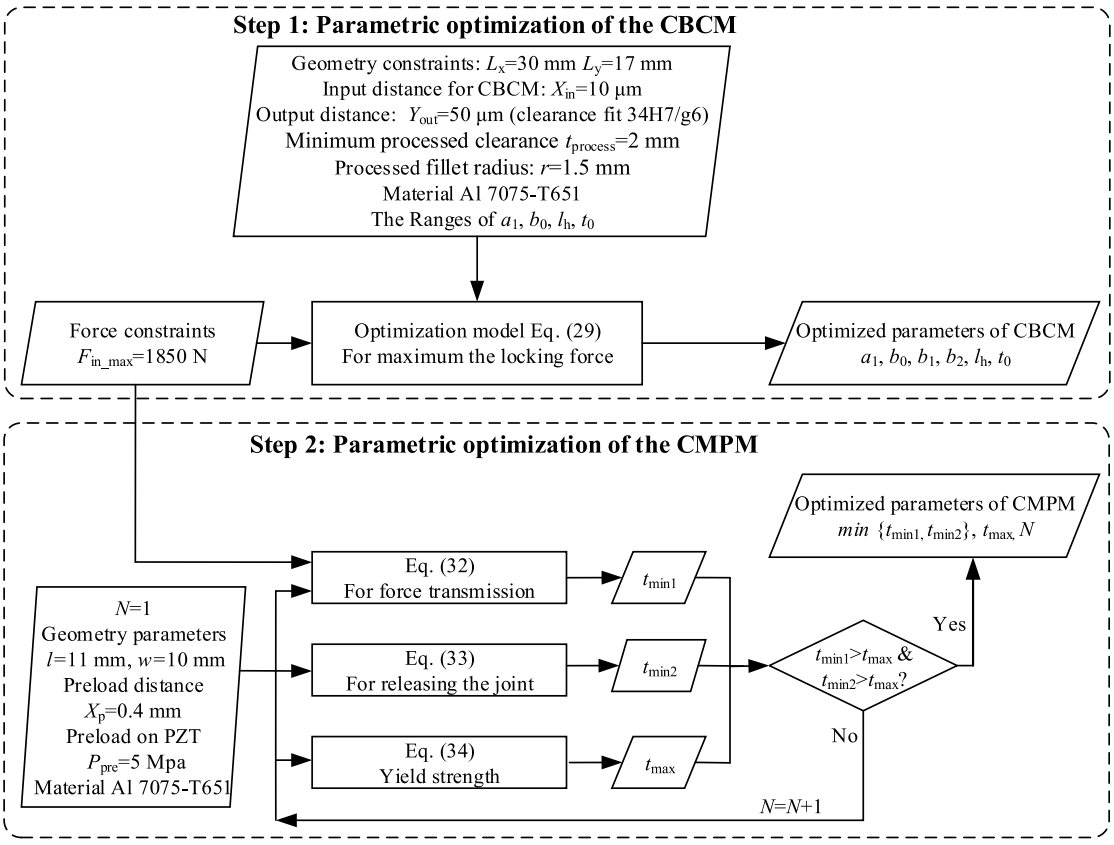

Fig. 12. Flowchart of the parametric optimization process for the inner CM.

each CMPM is $(X_p+c)/2$.

In addition, when the CMPM produces maximum deformation, its maximum stress should be smaller than the yield strength of the material. The maximal normal stress equation of the CMPM from [49] can be used and represented as

$$\sigma_{max2} = \left| 6 + \frac{0.06X_s^2}{\frac{t^2}{12} + \frac{1}{700}X_s^2} \frac{EtX_s}{2l^2} \right| + \left| \frac{0.6X_s^2}{\frac{t^2}{12} + \frac{X_s^2}{700}} \frac{Et^2}{12l^2} \right| < [\sigma] \tag{34}$$

where, X_s takes the value of $(X_p+c)/2$ since when the PZT output c displacement, the CMPM will generate maximum deformation.

Combining Eqs. (32)~(34), the minimum N and the range of the thickness of the flexible beam t can be obtained. The detailed process of the second step optimization is shown in Fig. 11. First, the parameters l, w, X_p, P_{pre}, $[\sigma]$ are given and set N=1. l, w can be estimated by the design space of the joint. X_p can be determined by the required preloading distance of the screw. Note that X_p cannot be too large since it will result in too much stress in the flexible beam. Otherwise, many basic CMPM groups with very thin flexible beams will be used to transmit a large force, which is difficult for processing. P_{pre} can be found in the instructions for the use of a pzt stack. Usually, for this non-high-dynamic application, it is relatively small.

As illustrated in Fig. 11, Eqs. (32) and (33) are used to calculate the minimum thickness of the flexible beam, and Eq. (34) is used to determine the maximum beam thickness of the flexible beam. If the feasible region to the three equations cannot be found simultaneously, N will be increased by one, and proceed to the next calculation. The loop will not stop until a feasible region for t is found. At last, the range of t and the minimum number of N will be output for guiding the design.

After the two-step optimization, the geometry parameters of the inner CM can be determined.

5. A design case with experimental verification

This section elaborates a design case by parametric optimization, which was fabricated and experimentally demonstrated. Some insights into improving the locking force are also discussed.

Table 3
Optimized parameters of the inner CM (unit: mm).

CBCM						CMPM	
a_1	b_0	b_1	b_2	l_h	t_0	t	N
8.98	2.00	1.01	5.99	5.00	0.99	1.216~1.341	3

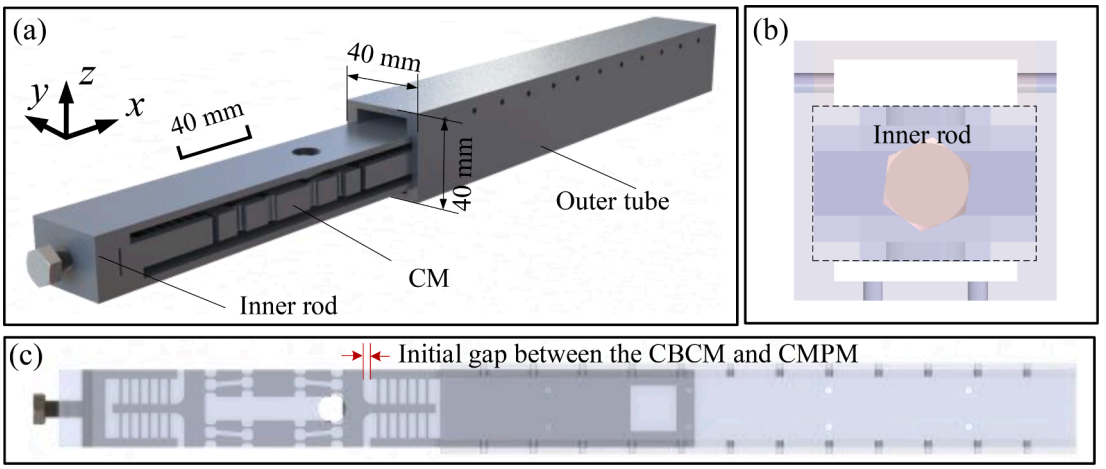

Fig. 13. The CAD model of the lockable P joint based on CNC machining uses the optimized parameters. (a) Axonometric view. (b) The side view of the joint with the outer tube and inner rod in the see-through state. (c) The vertical view of the joint with the outer tube and inner rod in the see-through state.

5.1. Parametric optimization of the inner CM

A design case based on CNC machining is presented in this section. The detailed parametric optimization process of the inner CM can be seen in the flowchart in Fig. 12.

For the first step optimization, the overall size constraints are given as $L_x = 30$ mm, $L_y = 17$ mm. The processed fillet radius is set as $r = 1.5$ mm. The minimum processed clearance between two rigid links is set as $t_{process} = 2$ mm. The 7075-T6 aluminum alloy ($E = 71$ Gpa $[\sigma] = 500$ Mpa) is used as the material for analysis. Considering the high axial stiffness of the CMPM will influence the output displacement of the PZT stack, the input displacement is set as $X_{in} = 10$ μm to retain some design margin. The input force constraint is set as $F_{in\_max} = 1850$ N. (For a commercial PZT stack, it can produce 65 μm free expansion (L_0) with 4000 N blocking force under 150 V voltage input with the overall size of 10 × 10 × 60 mm). The effective modulus of the elasticity of the piezoceramic martial is 36 N/mm^2.

Besides, the contact distance is set as $\Delta Y_{squeezed} = 40$ μm to ensure that the mechanism has enough contact distance with the outer tube. An economy processing accuracy determines the clearance between the inner CBCM and the outer tube. By looking up the Standard GB/T 1801-2009 (Limits and fits - Selection of tolerance zones and fits), a recommended clearance fit 34H7/g6 ($34_0^{+0.025}$ $34_{-0.025}^{-0.009}$) is chosen in mechanical manufacture, for which the maximum clearance is 0.05 mm and minimum clearance 0.009 mm. The minimum and maximum clearances can be used to calculate the maximum and minimum locking forces, respectively. The bounds of the variables are given as $a_1 \in [4, 8], b_0 \in [2, 3],\ l_h \in [5, 10],\ t_0 \in [0.6, 1.2]$. b_1 and b_2 are constrained by the design space constraint equations given in Eq. (29.d).

The optimization model in the first step is a nonlinear optimization problem with equality and inequality constraints (Eq. (29)). This model is solved by the sequential quadratic programming (SQP) method from the optimization toolbox in Maple 18. The optimized results of the CBCM are given in Table 3.

For the second step optimization, we set $l = 11$ mm and $w = 10$ mm. The initial pressure on the PZT stack is set as 5 Mpa. The preloading distance is given as $X_p = 0.4$ mm, which is 1/2 turn of an M5 coarse thread (Pitch = 0.8 mm). Through using the optimization process described in Fig. 12, the optimized range of thickness t and the number of groups N are also given in Table 3. The fabricated CMPM is recommended to use $t = 1.22$ mm near the lower end of the t range and will help to avoid material failure.

5.2. Prototype fabrication

Fig. 13 gives the CAD model of the P joint using the optimized design parameters based on CNC machining. Some holes are designed in the inner tube, and some larger gaps are reserved in the non-contact sides between the inner rod and the outer tube to facilitate the installation of the wires connected to the PZT stack (Figs. 13(a) and 14(c)). Besides, for large-stroke applications, the outer tube and

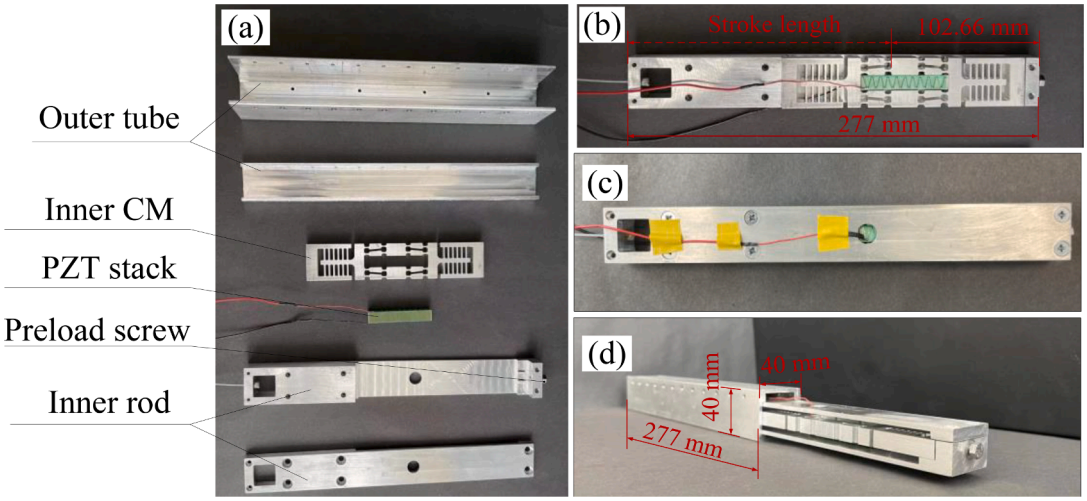

Fig. 14. The fabricated prototype. (a) Main parts of the prototype fabricated by CNC and the PZT stack actuation. (b) Assembly of the inner CM and the PZT stack. (c) Assembly of the inner rod. (d) The assembled lockable P joint.

inner rod can split into two parts (Figs. 13(b) and 14(a)) and be connected by bolts to facilitate CNC processing.

In manufacture, it is recommended that the gap between the frame of the CMPM and the CBCM (labeled in Fig. 13 (c)) is $X_p/2$ or slightly larger than $X_p/2$ to constrain the relative axial motion between the outer tube and inner rod caused by the external locking load. Note that under the locking load, though the CM could be deformed and produce the relative displacement/rotation between the outer tube and the inner rod, the main motion direction is along the axial direction (x-direction). In other directions, the displacement and rotation of the inner rod are constrained by the outer tube, as shown in Fig. 13(b).

In Appendix E, we also elaborate the approach to evaluating the relative axial displacement between the outer tube and inner rod under axial locking load. Numerical simulation results of the relative axial motion for the design case under locking load are also plotted in Fig. E.2 in Appendix. E with FEA verification. Since the inner CM is designed to have large axial stiffness to transmit axial preload from the screw, its axial displacement caused by the locking force is very small. From the results in Fig E.2, we can see that under the maximum load (350 N) that can be generated by setting $X_p = 0.4$ mm, $\mu = 1.2$, the relative axial displacement of the design case is just 14.2 μm.

Fig. 14(a) shows the main parts of the prototype processed by CNC according to the CAD model in Fig. 13. A commercial PZT stack (DCS3-101060 from Guangdong DC-Piezo Technology Co., Ltd.) is used to release the joint. Its key parameters are: width × height × length = 10 × 10 × 60 mm, blocking force = 4000 N, free expansion $L_0 = 65$ μm.

The assembling process includes several steps. At first, the PZT can be inserted into the CM and the preload screw is used to apply preload on the CM (Fig. 14(b) and (c)). Then, we can apply voltage on the PZT stack to facilitate the insertion of the inner rod into the outer tube to complete the overall assembly (Fig. 14(d)). Finally, we can cut off the power, and the joint will be automatically locked. Note that when assembling the PZT stack, the clearance between the inner CM and PZT stack has a significant effect on the locking force. This clearance can be adjusted by metal foil/washers with a very thin thickness (5 ~ 8 μm).

The overall size of the lockable joint (Figs. 13 and 14) is 40 × 40 × 277 mm in the fully contracted state, and its stroke length is 177.34 mm (Fig. 14(b)). More specifically, using the designed CM, the stroke length could be calculated by L_c-102.66 mm, where, L_c is the length of the joint when fully retracted. The proposed design is suitable for applications with large strokes.

5.3. Experimental verification

This section analyzes the locking performance of the design case and verifies its performance through experiments and nonlinear FEA. With knowing the preloading distance, the transmitted force of the CMPM imposed on CBCM can be obtained by substituting X_s=$X_p/2$ into Eq. (26), and the results can be further used to calculate the output force of the inner CM by Eq. (14). Then, the locking force can be calculated by F_L=$2\mu_1 F_{out}$. In the simulation, the clearances between the CMPM and outer tube are set as 50 μm and 9 μm (normally 9 ~ 50 μm for the chosen fit clearance 34H7/g6), using which we can obtain the minimum locking force and the maximum locking force, respectively.

Considering many factors could influence the coefficient of friction of the contacted surfaces [50], such as material, roughness, temperature, and lubrication, an inclined plane sliding experiment is conducted to roughly estimate the coefficient of friction used in this study. The tested friction coefficient is $\mu_1 = 0.31$ and the detailed experimental setup and process are shown in Appendix D.

In our design, the maximum preloading distance is set as 0.4 mm. We plotted the maximum and minimum locking force with respect to the preloading distance from 0.1 mm to 0.4 mm. The nonlinear FEA verification was also conducted with results shown in Fig.16. It can be observed that the theoretical results fit the FEA results well with an average error of 1.4%, which verifies the accuracy of the proposed model.

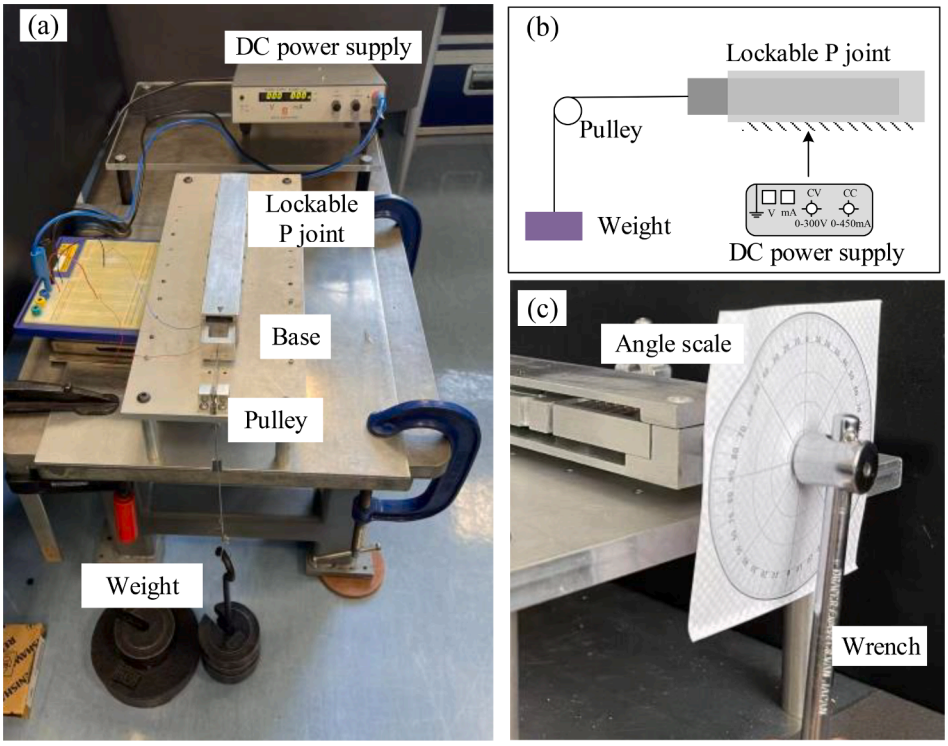

Fig. 15. Experimental setup to test locking force of the lockable joint. (a) Axonometric view of the experimental setup. (b) The schematic of the experiment. (c) Rotation angle adjustment of the preload screw.

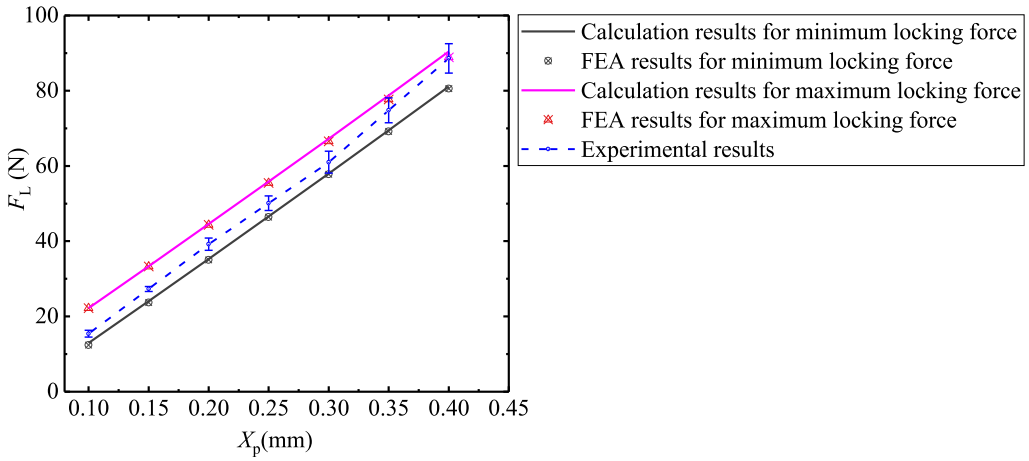

Fig. 16. The locking force of the design case under the coefficient of friction $\mu_1 = 0.31$: The maximum locking force was calculated by setting $Y_{out} =$ 9 μm, and the minimum locking force was calculated by setting $Y_{out} = 50$ μm. Experiments were run five times in each locking position. The mean locking force and the error bar (standard deviation) are plotted.

Fig. 15 shows the experimental setup to test the locking performance of the proposed joint. The desired preloading distance is determined by the rotation angle of the screw. The locking force is measured by the weight passing through the fixed pulley (Fig. 15(a) and (b)). A DC power supply (ES0300-0.45 from Delta Elektronika Co., Ltd.) is used to provide desired voltage input for the PZT actuation.

We used the angle scale on paper to measure the rotation angle of the screw (Fig. 15(c)). Although this is not very accurate for displacement control of the screw, it is valid for engineering applications since the preload force is not too sensitive to the rotation angle if the required rotation angle is relatively large. As discussed in Section 2.2, the design should allow for millimeter-level deformation in the axial direction to facilitate the adjustment of the preload. For this design, the preloading distance is set as 0.4

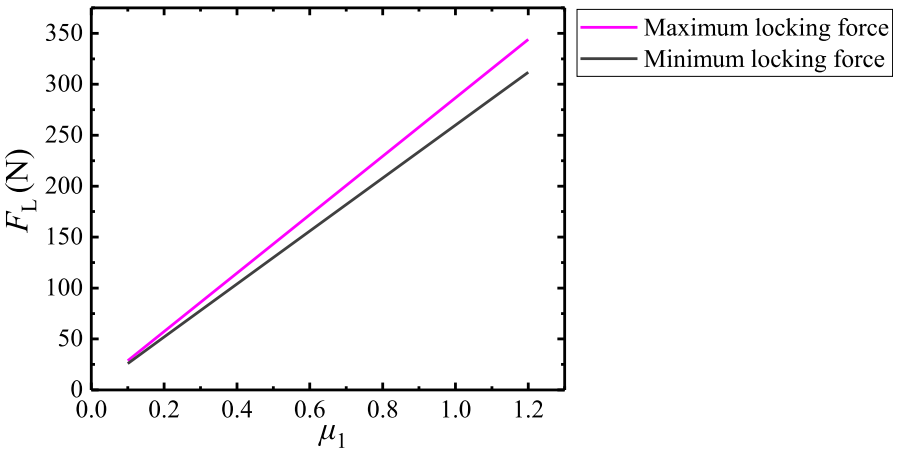

Fig. 17. Calculation results of the friction force for the design case under different friction coefficients with $X_p = 0.4$ mm.

mm which is 1/2 turn of the M5 coarse thread. The half-circle rotation is easy to be manually controlled. Alternatively, the preload screw can be replaced by a micrometer in future works to precisely control the preloading distance.

Experiments were run five times in each locking position. The average locking forces with the standard deviations are plotted in Fig. 16. It can be seen the magnitude of the mean experimental locking forces is between the calculated maximum and minimum forces, which indicates the validity of the proposed model. When the locking forces are relatively small, the experimental results are much closer to the theoretical minimum force. When the locking forces are relatively large, the experimental results are much closer to the theoretical maximum force. Besides, it can also be observed that with the increase of locking force, the standard deviation will also increase. We believe the error and the deviation of the experimental data are mainly affected by the structural deformation of the rigid part, which is ignored in the theoretical and FEA models, such as the external tube and the rigid links in the inner CM. In addition, the fitting clearance error and friction coefficient error at different positions caused by the machining process will also lead to some experimental errors.

It has been successfully observed that during all the experiments the locked joints can be released at voltages larger than 110 V (the allowable voltage of the PZT stack is -30 V ~ 150 V) with a recommended current of 60 mA. The results indicate that the lockable joint designed with the proposed model can reliably realize the PZT-based releasing function.

This paper has improved the locking force by optimizing the geometric parameters of the inner CM. Other approaches could be used in future works to improve the locking force while ensuring the releasing function. Two main methods are discussed here. First, a larger locking force could be obtained by a larger preloading distance. By doing this, higher strength materials are required to be used in prototype fabrication, and a different size/shape PZT stack with a larger blocking force could be used to release the joint (The PZT stacks can be customized in shapes and sizes through commercial companies). Second, the coefficient of friction between the two contacted surfaces can be increased. The most common way is to increase the roughness of the contact surfaces, which can be achieved by changing machining processes, adding additional machining processes (such as the etching process), or just adopting different materials.

The influence of the coefficient of friction on the locking force is shown in Fig. 17. The calculated maximum and minimum locking force of the design case are plotted with a preloading distance at $X_p = 0.4$ mm. It can be seen that by changing the coefficient of friction, the locking force can be significantly improved. The results also indicate that the proposed design is capable of achieving the expected lockable function with a relatively large locking force and an economic machining accuracy.

6. Conclusions

A novel compliant-mechanism-based modular lockable P joint is proposed in this study. It is constructed with a CBCM and a pair of CMPMs with PZT stack actuation. Due to the inherent merits of CMs and smart martial actuation, the present design has a compact structure with just five main parts (inner rod, outer tube, CM, PZT stack, preload screw). The joint is normally locked without energy consumption and could be released for passive moving. It is easy to assemble and scale up and down, serving for many potential applications such as morphing structures and parallel robots.

Analytical models are presented for the characteristics analysis of the substructures of the inner CM for locking applications. For the CBCM, the compliance matrix method is used to establish the kinetostatic model with various input and output conditions. For CMPM, the nonlinear deformation model is used for static analysis. Through case studies performed in the analytical model and FEA, it was shown the analytical model could effectively analyze the characteristics and predict the locking performance of the proposed design.

A two-step parametric optimization framework is proposed to improve its locking performance and ensure its releasing function. The first step is to optimize the geometry parameters of the CBCM with the comprehensive consideration of the motion and stiffness characteristics in the input/output motion directions as well as the constraints from design space, machine process, and yield strength of the material. The second step of optimization is for CMPM. An optimization method is proposed to determine the number of the basic

CMPM groups and the thickness of flexible beams. Using this method, the CMPM can transmit the required force with a desirable motion range and the joint can be released by PZT actuation.

An optimal design case is proposed along with its nonlinear FEA and experimental verification. The results indicate that the proposed design is capable of achieving the lockable function with a relatively large locking force and an economic machining accuracy.

Declaration of Competing Interest

The authors declare no conflict of interest in this paper.

Data availability

Data will be made available on request.

Acknowledgments

The authors would like to thank Mr. Tim Power, Mr. Michael O'Shea, Mr. Hilary Mansfield and Mr. James Griffiths for their help and advice in prototype fabrication and experiments. The first author is funded by the China Scholarship Council (CSC).

Supplementary materials

Supplementary material associated with this article can be found, in the online version, at doi:10.1016/j.mechmachtheory.2022.105083.

Appendix A

The compliance matrix of the flexure hinge uses the analytical formulas from Ref. [36], which is given as

$$\mathbf{C}_i = \begin{bmatrix} c_{\mathrm{x,F}} & 0 & 0 \\ 0 & c_{\mathrm{y,F}} & c_{\mathrm{y,M}} \\ 0 & c_{\theta,\mathrm{F}} & c_{\theta,\mathrm{M}} \end{bmatrix} = \begin{bmatrix} C_{\mathrm{a}} & 0 & 0 \\ 0 & C_{\mathrm{b,t}} + 2\alpha_{\mathrm{f}}(1+\mu)C_{\mathrm{a}} & -C_{\mathrm{b,c}} \\ 0 & -C_{\mathrm{b,c}} & C_{\mathrm{b,r}} \end{bmatrix} \tag{A.1}$$

in which α_{f} is a correction factor, which takes into account shear effects in the deformations of short flexure hinges and is approximated as $\alpha_{\mathrm{f}}= 6/5$ for rectangular cross-section [51]; μ is the Poisson's ratio of the material . The compliance parameters C_{a}, $C_{\mathrm{b,t}}$, $C_{\mathrm{b,c}}$, $C_{\mathrm{b,r}}$ in Eq. (A.1) can be calculated as

$$\begin{cases} C_{\mathrm{a}} = \dfrac{1}{Ew}\displaystyle\int_0^{l_{\mathrm{h}}} \frac{dx_{\mathrm{h}}}{t(x_{\mathrm{h}})} \\ C_{\mathrm{b,t}} = \dfrac{12}{Ew}\displaystyle\int_0^{l_{\mathrm{h}}} \frac{x_{\mathrm{h}}^2 dx_{\mathrm{h}}}{t(x_{\mathrm{h}})^3} \\ C_{\mathrm{b,c}} = \dfrac{12}{Ew}\displaystyle\int_0^{l_{\mathrm{h}}} \frac{x_{\mathrm{h}} dx_{\mathrm{h}}}{t(x_h)^3} \\ C_{\mathrm{b,r}} = \dfrac{12}{Ew}\displaystyle\int_0^{l_{\mathrm{h}}} \frac{dx_{\mathrm{h}}}{t(x_{\mathrm{h}})^3} \end{cases} \tag{A.2}$$

where, E is Young's modulus of the material, w is the width of the hinge, l_{h} is the length of the hinge, $t(x_{\mathrm{h}})$ is the thickness of the hinge at point x_{h}. For a corner-filleted hinge shown in Fig. 5(b), $t(x_{\mathrm{h}})$ can be expressed as

$$t(x_{\mathrm{h}}) = \begin{cases} -2\left(\sqrt{r^2 - (x_{\mathrm{h}} - r)^2} + 2r + t_0, x_{\mathrm{h}} \in (0, r)\right. \\ t_0, x_{\mathrm{h}} \in (r, l_{\mathrm{h}} - r) \\ -2\sqrt{r^2 - (x_{\mathrm{h}} - l_{\mathrm{h}} + r)^2} + 2r + t_0, x_{\mathrm{h}} \in (l_{\mathrm{h}} - r, l_{\mathrm{h}}) \end{cases} \tag{A.3}$$

Appendix B

This section gives the formula derivations for calculating the displacement (x_h, y_h, θ_h) of the free end of the flexure hinge in CBCM. Fig. B1 shows the initial and deformed state of one limb of the CBCM.

In the initial state, the inclination angle of the limb can be estimated by

$$\theta = \arctan\left(\frac{b_1}{L_x - a_1}\right) \tag{B.1}$$

In the deformed state, the inclination angle of the limb can be estimated by

$$\theta^* = \arctan\left(\frac{Y_{out}/2 + b_1}{L_x - a_1 - X_{in}/2}\right) \tag{B.2}$$

Hence, using the above results, the displacement of the flexure hinge can be derived as

$$\begin{aligned} \theta_h &= \theta^* - \theta \\ x_h &= \frac{X_{in}/2 - l_r(\cos\theta - \cos\theta^*)}{2} \\ y_h &= \frac{Y_{out}/2 - l_r(\sin\theta^* - \sin\theta)}{2} \end{aligned} \tag{B.3}$$

in which l_r is the length of the rigid link labeled in Fig. B1.

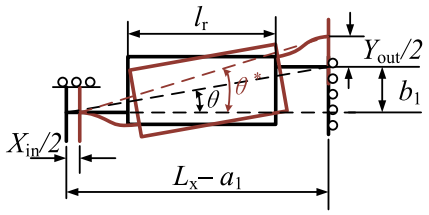

Fig. B1. Initial and deformed state of one limb of the CBCM.

Appendix C

This section provides the stress concentration factors calculation formulas. For circular-fillet flexure hinges with the ratio of fillet radius to minimum thickness (r/t_0) ranging from 0.5 to 2, the stress concentration factors k_b for bending, and k_t for tension in Eq. (30) can be calculated by the following empirical expressions [48]

$$k_t = -0.1729\left(\frac{r}{t_0}\right)^3 + 0.8539\left(\frac{r}{t_0}\right)^2 - 1.4265\left(\frac{r}{t_0}\right) + 1.9613 \tag{C.1}$$

$$k_b = 0.1721\left(\frac{r}{t_0}\right)^4 - 0.9288\left(\frac{r}{t_0}\right)^3 + 1.8387\left(\frac{r}{t_0}\right)^2 - 1.6593\left(\frac{r}{t_0}\right) + 1.669 \tag{C.2}$$

Appendix D

An inclined plane sliding experiment is conducted to estimate the coefficient of friction of the prototype. We place the compliant mechanism on a plane whose slope can be adjusted through a lifting table. When the compliant mechanism can slide on the plane, we record the height of the plate h_p. Then, the coefficient of friction can be calculated as

$$\mu_1 = \tan(\alpha_p) = \frac{h_p}{\sqrt{l_p^2 - h_p^2}} \tag{D.1}$$

in which σ_p is the angle of the plate, $l_p = 4025$ mm is the length of the plane, h_p is the height of the right side of the plane which is measured by a vernier scale, as shown in Fig. D.1 (b).

The experiment was repeated 5 times. The average angle of the plane α_p is 17.1° and the calculated coefficient of friction is 0.31.

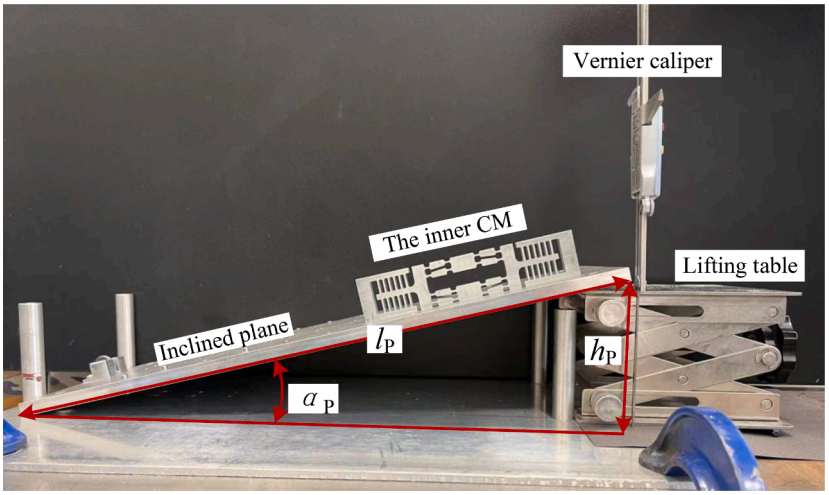

Fig. D.1. The inclined plane experiment for obtaining the coefficient of friction.

Appendix E

This section gives the method to analyze the relative axial motion between the outer tube and inner rod under the axial locking load. When the joint is in the locking state, the motion stage of the CBCM is fixed with the outer tube. Hence, the motion of the outer tube is the same as that of the CBCM.

Note that, when computing the axial motion of the outer tube, the axial deformation of CBCM is neglected since the axial stiffness of CBCM is much larger than that of the CMPM (As discussed in Section 2.2, under the preload force, the CMPM is designed to generate millimeter-level deformation to facilitate the adjustment of preload, and the CBCM is designed to generate tens of microns deformation to facilitate PZT-stack-based actuation).

Referring to Fig. E.1(a), when the joint is locked with no external locking load, the two CMPMs could generate equal axial deformation $X_P/2$ and equal compress force F_{gP}. If we represent Eq. (26) as a more concise form

$$F_g = f(X_s), \tag{E.1}$$

F_{gp} can be calculated as $F_{gp} = f(X_P/2)$, where X_p is the preloading distance of the preload screw.

Referring to Fig. E.1(b), if the joint is locked under axial locking load F_L along the *-x* direction, the CBCM will produce an axial displacement Δ_{AM}. The axial deformation of CMPMs on the left side and right side are $X_P/2+\Delta_{AM}$ and $X_P/2-\Delta_{AM}$, respectively. Then the axial force from CMPM on the two sides of the CBCM can be derived as

$$\begin{aligned} F_{gL} &= f\left(X_p/2 + \Delta_{AM}\right) \\ F_{gR} &= f\left(X_p/2 - \Delta_{AM}\right) \end{aligned} \tag{E.2}$$

Hence, the static equilibrium equation of CBCM can be written as

$$F_{gL} = F_L + F_{gR} \rightarrow f\left(X_p/2 + \Delta_{AM}\right) = F_L + f\left(X_p/2 - \Delta_{AM}\right) \tag{E.3}$$

Through solving Eq. (E.3), the axial displacement Δ_{AM} can be obtained.

The axial displacement of the design case in Section 5 is plotted in Fig. E.2 with nonlinear FEA verification. It is shown that the proposed model is very accurate with a maximum error of less than 0.1% compared with the FEA results. Under the maximum load (350 N) that can be generated by setting $X_p = 0.4$ mm, $\mu = 1.2$, the axial displacement of the design case is just 14.2 μm.

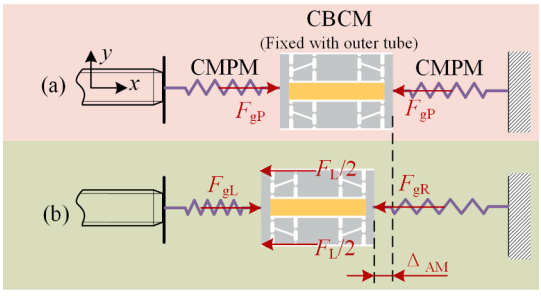

Fig. E.1. Relative axial displacement between the outer tube and inner rod under axial locking load (assuming the inner rod is fixed). (a) Locking state with no external axial load. (b) Locking state with external axial load.

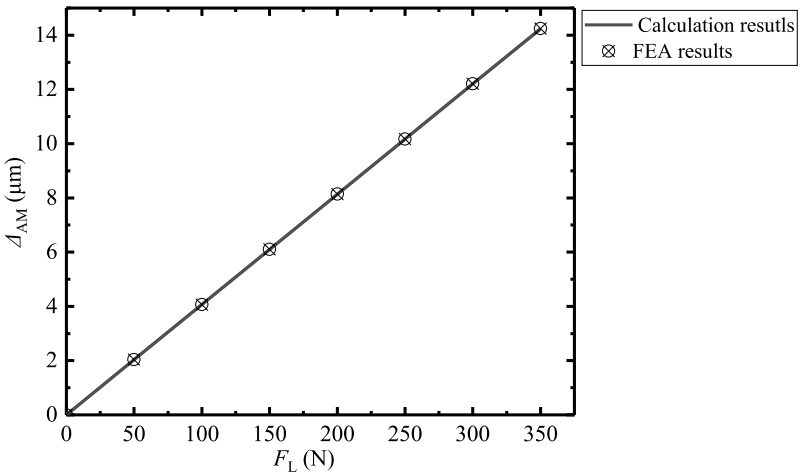

Fig. E.2. Relative axial displacement between the external tube and inner rod of the design case in Section 5 under external locking load. (The maximum force 350 N is from Fig. 14 by setting $X_p = 0.4$ mm, $\mu = 1.2$, $Y_{out} = 9$ μm).

References

[1] M. Plooij, G. Mathijssen, P. Cherelle, D. Lefeber, B. Vanderborght, Lock your robot: a review of locking devices in robotics, IEEE Robot. Autom. Mag. 22 (1) (2015) 106–117.
[2] F. Xi, Y. Zhao, J. Wang, W. Wang, Y. Tian, Two Actuation methods for a complete morphing system composed of a VGTM and a compliant parallel mechanism, J. Mech. Robot. 13 (2) (2021), 021020.
[3] A. Moosavian, F. Xi, S.M. Hashemi, Design and motion control of fully variable morphing wings, J. Aircr. 50 (4) (2013) 1189–1201.
[4] A. Moosavian, F. Xi, Holonomic under-actuation of parallel robots with topological reconfiguration, Mech. Mach. Theory 96 (2016) 290–307.
[5] F. Aghili, K. Parsa, A reconfigurable robot with lockable cylindrical joints, IEEE Trans. Robot. 25 (4) (2009) 785–797.
[6] S. Lu, Z. Ahmad, M. Zoppi, X. Ding, D. Zlatanov, R. Molfino, Design and testing of a highly reconfigurable fixture with lockable robotic arms, J. Mech. Des. 138 (8) (2016), 085001.
[7] R. Lin, W. Guo, Type synthesis of reconfiguration parallel mechanisms transforming between trusses and mechanisms based on friction self-locking composite joints, Mech. Mach. Theory 168 (2022), 104597.
[8] Y. Tian, Y. Zhao, L. Li, G. Yuan, F. Xi, Design and analysis of a multi-segment shape morphing mechanism, J. Mech. Robot. 13 (2) (2020), 021004.
[9] C.J. Pennycuick, The flight of petrels and albatrosses (Procellariiformes), observed in South Georgia and its vicinity, Philos. Trans. R. Soc. Lond. B Biol. Sci. 300 (1098) (1982) 75–106.
[10] G. Sachs, J. Traugott, A.P. Nesterova, G. Dell'Omo, F. Kummeth, W. Heidrich, A.L. Vyssotski, F. Bonadonna, Flying at no mechanical energy cost: disclosing the secret of wandering albatrosses, PLOS One 7 (9) (2012) e41449.
[11] D.G. Chung, J. Kim, D. Baek, J. Kim, D.S. Kwon, Shape-locking mechanism of flexible joint using mechanical latch with electromagnetic force, IEEE Robot. Autom. Lett. 4 (3) (2019) 2661–2668.
[12] B. Brackx, M. Van Damme, A. Matthys, B. Vanderborght, D. Lefeber, Passive ankle-foot prosthesis prototype with extended push-off, Int. J. Adv. Robot. Syst. 10 (2) (2013) 101.
[13] A. Moosavian, M. Rizoiu, F. Xi, Design of a multifunctional flow control valve for self-circulating hydraulic cylinders, J. Press. Vessel Technol. 139 (2) (2017), 025001.
[14] F. Aghili, K. Parsa, Design of a reconfigurable space robot with lockable telescopic joints, in: Proceedings of the 2006 IEEE/RSJ International Conference on Intelligent Robots and Systems, Beijing, China, IEEE, 2006, pp. 4608–4614.
[15] S. Lu, M. Zoppi, D. Zlatanov, Z. Ahmad, R. Molfino, Design and testing of a novel stepless lockable joint for use in reconfigurable fixtures, in: Proceedings of the International Design Engineering Technical Conferences and Computers and Information in Engineering Conference, American Society of Mechanical Engineers, 2014. V05BT08A025.
[16] G.V. Oort, R. Carloni, D.J. Borgerink, S. Stramigioli, An energy efficient knee locking mechanism for a dynamically walking robot, in: Proceedings of the 2011 IEEE International Conference on Robotics and Automation, Shanghai,China, 2011, pp. 2003–2008.
[17] X. Lan, L. Liu, F. Zhang, Z. Liu, L. Wang, Q. Li, F. Peng, S. Hao, W. Dai, X. Wan, World's first spaceflight on-orbit demonstration of a flexible solar array system based on shape memory polymer composites, Sci. China Technol. Sci. 63 (8) (2020) 1436–1451.
[18] D. Zhang, L. Liu, J. Leng, Y. Liu, Ultra-light release device integrated with screen-printed heaters for CubeSat's deployable solar arrays, Compos. Struct. 232 (2020), 111561.
[19] G. Mathijssen, D. Lefeber, B. Vanderborght, Variable recruitment of parallel elastic elements: series–parallel elastic actuators (SPEA) with dephased mutilated gears, IEEE/ASME Trans. Mechatron. 20 (2) (2014) 594–602.
[20] P. Cherelle, V. Grosu, A. Matthys, B. Vanderborght, D. Lefeber, Design and validation of the ankle mimicking prosthetic (AMP-) foot 2.0, IEEE Trans. Neural Syst. Rehabil. Eng. 22 (1) (2013) 138–148.
[21] G. Van Oort, R. Carloni, D.J. Borgerink, S. Stramigioli, An energy efficient knee locking mechanism for a dynamically walking robot, in: Proceedings of the 2011 IEEE International Conference on Robotics and Automation, IEEE, 2011, pp. 2003–2008.
[22] E.J. Rouse, L.M. Mooney, H.M. Herr, Clutchable series-elastic actuator: implications for prosthetic knee design, Int. J. Robot. Res. 33 (13) (2014) 1611–1625.
[23] Y. Tian, Z. Tian, Y. Zhao, L. Li, F. Xi, Design and analysis of a passive lockable prismatic joint for reconfigurable mechanisms, in: Proceedings of the 5th IEEE/IFToMM International Conference on Reconfigurable Mechanisms and Robots, Toronto, Canada, 2021.
[24] X. Guo, W. Li, Q. Gao, H. Yan, Y. Fei, W. Zhang, Self-locking mechanism for variable stiffness rigid–soft gripper, Smart Mater. Struct. 29 (3) (2020), 035033.
[25] C. Yang, S. Geng, I. Walker, D.T. Branson, J. Liu, J.S. Dai, R. Kang, Geometric constraint-based modeling and analysis of a novel continuum robot with shape memory alloy initiated variable stiffness, Int. J. Robot. Res. 39 (14) (2020) 1620–1634.
[26] J.M. Porta, F. Thomas, Closed-form position analysis of variable geometry trusses, Mech. Mach. Theory 109 (2017) 14–21.
[27] A. Spinos, D. Carroll, T. Kientz, M. Yim, Topological reconfiguration planning for a variable topology truss, J. Mech. Robot. 13 (4) (2021), 040902.
[28] Y.D. Patel, P.M. George, Parallel manipulators applications—a survey, Modern Mech. Eng. 02 (03) (2012) 57–64.
[29] Y. Zhao, F. Xi, Y. Tian, W. Wang, L. Li, Design of a planar hyper-redundant lockable mechanism for shape morphing using a centralized actuation method, Mech. Mach. Theory 165 (2021), 104439.

[30] Larry L. Howell, Spencer P. Magleby, B.M. Olsen, Handbook of Compliant Mechanisms, Wiley, New York, 2013.
[31] Q. Xu, Y. Li, Analytical modeling, optimization and testing of a compound bridge-type compliant displacement amplifier, Mech. Mach. Theory 46 (2) (2011) 183–200.
[32] G. Hao, H. Li, Nonlinear analytical modeling and characteristic analysis of a class of compound multibeam parallelogram mechanisms, J. Mech. Robot. 7 (4) (2015), 041016.
[33] W. Dong, F. Chen, F. Gao, M. Yang, L. Sun, Z. Du, J. Tang, D. Zhang, Development and analysis of a bridge-lever-type displacement amplifier based on hybrid flexure hinges, Precis. Eng. 54 (2018) 171–181.
[34] S. Noveanu, N. Lobontiu, J. Lazaro, D. Mandru, Substructure compliance matrix model of planar branched flexure-hinge mechanisms: design, testing and characterization of a gripper, Mech. Mach. Theory 91 (2015) 1–20.
[35] Y. Yong, S.R. Moheimani, B.J. Kenton, K. Leang, Invited review article: high-speed flexure-guided nanopositioning: mechanical design and control issues, Rev. Sci. Instrum. 83 (12) (2012), 121101.
[36] N. Lobontiu, Compliance-based matrix method for modeling the quasi-static response of planar serial flexure-hinge mechanisms, Precis. Eng. 38 (3) (2014) 639–650.
[37] J. Cao, M. Ling, D.J. Inman, J. Lin, Generalized constitutive equations for piezoactuated compliant mechanism, Smart Mater. Struct. 25 (9) (2016), 095005.
[38] M. Ling, L.L. Howell, J. Cao, G. Chen, Kinetostatic and dynamic modeling of flexure-based compliant mechanisms: a survey, Appl. Mech. Rev. 72 (3) (2020), 030802.
[39] N. Lobontiu, J.S. Paine, E. Garcia, M. Goldfarb, Design of symmetric conic-section flexure hinges based on closed-form compliance equations, Mech. Mach. Theory 37 (5) (2002) 477–498.
[40] G. Chen, X. Liu, H. Gao, J. Jia, A generalized model for conic flexure hinges, Rev. Sci. Instrum. 80 (5) (2009), 055106.
[41] Q. Meng, Y. Li, J. Xu, New empirical stiffness equations for corner-filleted flexure hinges, Mech. Sci. 4 (2) (2013) 345–356.
[42] T. Li, J. Zhang, Y. Jiang, Derivation of empirical compliance equations for circular flexure hinge considering the effect of stress concentration, Int. J. Precis. Eng. Manuf. 16 (8) (2015) 1735–1743.
[43] N. Lobontiu, J.S. Paine, E. Garcia, M. Goldfarb, Corner-filleted flexure hinges, J. Mech. Des. 123 (3) (2001) 346–352.
[44] A.H. Meitzler, D. Berlincourt, F.S. Welsh, H.F. Tiersten, G.A. Coquin, A.W. Warner, IEEE Standard on Piezoelectricity, IEEE, 1988.
[45] R.T. Barrett, Fastener Design Manual NASA Reference Publication 1228, NASA, Washington, DC, 1990, p. 16.
[46] W.D. Pilkey, D.F. Pilkey, Z. Bi, Peterson's Stress Concentration Factors, John Wiley & Sons, 2020.
[47] G. Chen, J. Wang, X. Liu, Generalized equations for estimating stress concentration factors of various notch flexure hinges, J. Mech. Des. 136 (3) (2014), 031009.
[48] L. Hale, Principles and Techniques for Designing Precision Machines, Massachusetts Institute of Technology, 2000 (Chapter 6).
[49] G. Hao, H. Li, Extended static modeling and analysis of compliant compound parallelogram mechanisms considering the initial internal axial force*, J. Mech. Robot. 8 (4) (2016), 041008.
[50] S. Sardar, S. Kumar Karmakar, D. Das, Tribological properties of Al 7075 alloy and 7075/Al2O3 composite under two-body abrasion: a statistical approach, J. Tribol. 140 (5) (2018), 051602.
[51] W.C. Young, R.G. Budynas, A.M. Sadegh, Roark's Formulas for Stress and Strain, McGraw-hill, New York, 2002.